Zheng, B.-T., & Teng, J.-G. (2023). Finite-Element Modeling of FRP-Confined Noncircular Concrete Columns Using the Evolutionary Potential-Surface Trace Plasticity Constitutive Model for Concrete. Journal of Composites for Construction, 27(1), 04022089.

Finite element modeling of FRP-confined non-circular concrete columns using the evolutionary potential-surface trace plasticity constitutive model for concrete

Bo-Tong Zheng[a] and Jin-Guang Teng, F.ASCE[b]*

[a] *Research Assistant Professor, Department of Civil and Environmental Engineering, The Hong Kong Polytechnic University, Hong Kong, China, Email: btzheng@polyu.edu.hk*

[b] *Chair Professor of Structural Engineering, Department of Civil and Environmental Engineering, The Hong Kong Polytechnic University, Hong Kong, China, Email: cejgteng@polyu.edu.hk*

**Corresponding author*

Abstract

The compressive behavior of fiber-reinforced polymer (FRP)-confined concrete columns with a non-circular cross-section has been investigated through extensive experimental, analytical, and numerical research, but a unified theoretical/numerical approach that can accurately predict both their section-average behavior and local concrete behavior is not yet available. In non-circular columns under axial compression, the concrete is typically under a non-uniform stress state of three-dimensional (3D) compression, with the lateral compressive stresses being the reactive stresses from the confining device (i.e., passive confinement). The authors of the present paper recently developed a plasticity constitutive model for concrete under general 3D compressive stresses, which possesses a potential surface with an evolutionary deviatoric trace that can accurately capture the results of existing compression tests of concrete cubes under non-uniform, passive confinement. This paper explores the application and capability of this evolutionary potential-surface trace (EPT) plasticity constitutive model in the finite element (FE) analysis of FRP-confined square, rectangular, and elliptical plain-concrete columns under concentric compression. The section-average behavior of all the selected non-circular columns predicted by these FE analyses is close to the existing experimental data. The numerical results obtained with the EPT plasticity constitutive model

are then examined in detail to achieve an improved understanding of local concrete behavior in FRP-confined non-circular columns.

Keywords: FRP, concrete, plasticity constitutive model, non-circular column, non-uniform confinement, axial compression, finite element modeling.

Introduction

To make full use of fiber-reinforced polymer (FRP) composites in the construction of new concrete columns and the strengthening of existing concrete columns, extensive experimental and analytical research has been conducted on FRP-confined concrete columns under concentric compression (e.g., Saadatmanesh et al. 1994; Mirmiran and Shahawy 1997; Pessiki et al. 2001; Lam and Teng 2003a; Jiang and Teng 2007; Wei and Wu 2012; Lim and Ozbakkaloglu 2015; Lin and Teng 2020). It has been a consensus for some time that the behavior of FRP-confined concrete columns with a circular cross-section (referred to as circular columns hereafter for brevity) is sufficiently well understood and can be accurately predicted with some of the analytical stress-strain models (e.g., Jiang and Teng 2007; Teng et al. 2007; Teng et al. 2009). However, much less has been achieved in understanding and predicting the behavior of FRP-confined concrete columns with a non-circular cross-section, including square, rectangular, and elliptical cross-sections (referred to as non-circular columns hereafter for brevity) (e.g., Mirmiran et al. 1998; Rochette and Labossière 2000; Pessiki et al. 2001; Lam and Teng 2003b; Wang and Wu 2008; Ozbakkaloglu 2013; Lin and Teng 2020).

In FRP-confined circular concrete columns, the concrete is deemed to be uniformly confined with FRP: that is, the concrete at all locations of the section receives the same confining stress and hence exhibits the same axial stress-strain behavior, and the experimentally measured average axial stress-axial strain behavior directly reflects the local response of concrete. By contrast, the concrete in FRP-confined non-circular columns is under non-uniform confinement: the concrete at different locations of a section receives different confining stresses and hence exhibits different axial stress-axial strain responses; the non-uniformity of confinement also increases with the axial deformation. The experimentally measured section-average axial stress-axial strain behavior is a mere aggregate of, but is unable to reflect, the different local concrete behaviors across the section. Therefore, knowledge of local concrete behavior in FRP-confined non-circular columns beyond what is offered by existing experimental data is needed to better understand and more accurately predict the behavior of FRP-confined non-circular concrete columns.

The ‘arching effect’ concept is widely used to conceptualize with the non-uniform confining stress distribution over the section of an FRP-confined non-circular concrete column, in which the non-circular section is partitioned into a region with effective confinement and the remainder of the section with negligible confinement (e.g., Sheikh and Uzumeri 1980; Mander et al. 1988; Teng and Lam 2002). This binary, static oversimplification is somewhat intuitive rather than being based on rigorous analysis/evidence. In order to experimentally identify the effectively confined region within the section, the local concrete stresses need to be measured across the section throughout the loading process, as attempted by Teng et al. (2015a) via the use of a pressure mapping system; more work is needed in order to achieve accurate measurements of these local stresses (see Appendix A). Moreover, some insight into the variation of local concrete confinement over the section at the final stage can be obtained by scrutinizing the failure pattern of crushed FRP-confined concrete columns, such as those reported in Ozbakkaloglu and Oehlers (2008), Wang and Wu (2008), Wu and Wei (2010), Ozbakkaloglu (2013), and Shan et al. (2019). However, more experimental data and analyses are required to establish a good understanding of the local behavior of concrete in a non-uniformly confined member. Therefore, three-dimensional (3D) finite element (FE) analysis has been seen as the more reliable alternative to gain knowledge of local concrete behavior in FRP-confined non-circular columns. The accuracy of an FE simulation is mainly dependent on the accuracy of the constitutive model employed for the concrete; more specifically, for the accurate modeling of FRP-confined non-circular concrete columns, a constitutive model suitable for concrete under non-uniform, passive confinement is necessary.

While many FE studies have been carried out on FRP-confined circular columns (e.g., Mirmiran et al. 2000; Shahawy et al. 2000; Yu et al. 2010a;b; Teng et al. 2015b; Lin and Teng 2017; Ribeiro et al. 2019), FE studies of non-circular columns, as mentioned below, have been limited mainly due to the lack of a competent concrete constitutive model. In some of the FE analyses of FRP-confined square columns (Nisticò and Monti 2013; Nisticò 2014), the concrete was simulated as a linear-elastic material, which is obviously inaccurate. In the other studies involving FE analysis of FRP-confined square, rectangular, or elliptical columns (Doran et al. 2009; Yu et al. 2010b; Hajsadeghi et al. 2011; Yeh and Chang 2012; Mostofinejad et al. 2015; Hany et al. 2016; Teng et al. 2016; Lin and Teng 2020; Fanaradelli and Rousakis 2020; Ekop and Grassl 2022), the concrete was simulated using plasticity-based constitutive models, which, though capable of depicting the full 3D incremental stress-strain relationship of confined concrete, are inaccurate for concrete under substantially non-uniform, passive confinement as discussed below.

Available plasticity models for concrete have been formulated mainly on the basis of experimental data for concrete under active stresses (e.g., Han and Chen 1985; Lubliner et al. 1989; Lee and Fenves 1998; Grassl et al. 2002) and are thus inaccurate for concrete under passive confinement. In order to overcome this weakness that compromises the capability of plasticity models for predicting the behavior of passively-confined concrete, the behavior of FRP-confined concrete as interpreted from experimental data was incorporated into the existing framework of, mainly the Drucker-Prager (D-P) type, plasticity models in a series of studies before 2010 (e.g., Mirmiran et al. 2000; Shahawy et al. 2000; Karabinis and Rousakis 2002; Rousakis et al. 2008). The limitations of these modified plasticity constitutive models proposed in these studies were subsequently resolved by a more appropriate approach proposed by Yu et al. (2010a; b), which incorporated the analytical stress-strain model of Teng et al. (2007) for concrete under uniform FRP (i.e., passive) confinement into the built-in plasticity models of ABAQUS (version 6.5). Models adopting this approach, referred to as analytically-augmented (AA) plasticity models herein, are capable of close prediction of the behavior of concrete under both uniform-active and uniform-passive confinement and have also been widely employed in modeling the behavior of FRP-confined non-circular concrete columns either directly or by tuning the core analytical stress-strain model (e.g., Jiang and Wu 2012; Mostofinejad et al. 2015; Mazzucco et al. 2016; Lin and Teng 2017; Mohammadi et al. 2019).

However, these AA plasticity models are still inaccurate for concrete under substantially non-uniform FRP confinement as the non-uniform confinement in these models is only indirectly accounted for by the empirical adaptation of an analytical stress-strain model (the core analytical model) developed on the basis of experimental data of concrete under uniform, passive confinement (e.g., Lam and Teng 2004; Lam et al. 2006). In Yu et al. (2010b), which pioneered the AA type of models, both a section level approximation (referred to as method I) and a local level approximation (referred to as method II) were explored for this empirical adaptation. Only the local approximation method, which relies on the conversion of non-uniform confining stresses into an equivalent uniform confining pressure and the definition of an equivalent lateral/hoop strain, is considered in the present study, as the section level method, which assumes the same flow rule for the entire section, is less reliable (Yu et al. 2010b). Even with the local approach, the empirical conversion approach explored by Yu et al. (2010b) and followed by many other researchers (e.g., Mostofinejad et al. 2015; Lin and Teng 2017; Mohammadi et al. 2019) fails to capture the behavioral characteristics of concrete under substantially non-uniform passive confinement, as demonstrated by (Zheng and Teng 2022a).

The development of a more capable constitutive model for concrete subjected to substantially non-uniform confinement requires relevant experimental data. The dilation behavior of concrete under uniform confinement has been well established through compression tests of concrete cylinders under hydrostatic pressure (Hoek cell tests) for active confinement, as summarized by Samani and Attard (2014), and through those with external FRP confinement for passive confinement, as summarized by (Lim and Ozbakkaloglu 2015a). However, equally direct data for the deformation behavior of concrete under non-uniform passive confinement has not been available until the compression tests of 100 mm or 150 mm concrete cubes conducted by Jiang et al. (2017) and Mohammadi and Wu (2017), respectively, where the cubes were confined with lateral confining devices of unequal stiffnesses in the two directions. These tests provided valuable data germane to the local behavior of concrete in an FRP-confined non-circular column, which complement the available test data for concrete under uniform confinement.

The authors of the present paper analyzed the comprehensive dataset assembled from Jiang et al. (2017), Lim and Ozbakkaloglu (2015b), Mohammadi and Wu (2017), Piscesa et al. (2016), and Samani and Attard (2014), and arrived at a unified interpretation of the deformation behavior of concrete (Zheng and Teng 2022a). However, it was found that the new interpretation cannot be represented by the widely adopted framework of the D-P type plasticity models, including that of the AA plasticity models, which employ a fundamentally unsuitable potential surface incapable of accurately depicting the deformation behavior of concrete under non-uniform confinement. Indeed, the authors who conducted the new category of tests have proposed new AA models based on the new datasets in a series of works (Mohammadi et al. 2019; Mohammadi and Wu 2019; Li et al. 2021); these new AA models are still unable to accurately reproduce the test results of concrete cubes under non-uniform, passive confinement, as discussed in Zheng and Teng (2022a).

Therefore, a new plasticity model incorporating a potential surface with an evolutionary deviatoric trace specifically devised to represent the unified interpretation of confined concrete behavior was proposed by the authors of the present work (Zheng and Teng 2022a); the accuracy of this new model for concrete under active confinement, uniform passive confinement, and non-uniform passive confinement was validated at the material level in that study. The purpose of the present study is twofold. The first is to further evaluate the performance of the evolutionary potential-surface trace (EPT) plasticity constitutive model at the structural member level by simulating FRP-confined non-circular columns and comparing the predictions of section-average behavior with available experimental data. Secondly, the predictions of local concrete behavior obtained with the EPT model are used to advance the understanding of confinement mechanisms in FRP-confined non-circular concrete columns. It should be noted that the study has previously been briefly reported elsewhere (Zheng and Teng 2022b).

The evolutionary potential-surface trace (EPT) plasticity constitutive model

Mathematical formulation

The newly proposed EPT plasticity constitutive model is expounded in Zheng and Teng (2022a), and a brief summary of the critical components is presented here. The model is based on rate-independent incremental elastoplasticity, with stress and strain tensors represented in the Haigh–Westergaard coordinate system. The fundamental assumption of the EPT model is that different concrete materials share the same qualitative descriptors for the stress and the deformation behaviors, but these descriptors can be quantitatively different for each physically unique concrete (as determined by a particular combination of constituent raw materials and production process giving a unique set of material property values). Accordingly, the EPT model employs appropriate mathematical equations for the descriptors (e.g., yield surface, potential surface, and hardening rule) while using different values for the material parameters embedded in these descriptors to reflect quantitative differences. It should be emphasized that for the same concrete, the values of the material parameters remain the same regardless of the nature/level of confinement; the model thus possesses the necessary robustness for the simulation of non-uniformly confined concrete members where the concrete at different locations is subjected to different confining conditions. It is therefore obvious that the values of the material parameters of the EPT model for a given concrete can be calibrated from one state (e.g., under uniform confinement) of the concrete and then used to predict its behavior in another state (e.g., under non-uniform confinement).

The model employs the widely used strength surface proposed by Menetrey and Willam (1995) and the associated open yield surfaces that are reduced from the strength surface (Papanikolaou and Kappos 2007), leading to the following expression for the yield surfaces:

$$f(\xi,\rho,\theta;\kappa)=\left(\sqrt{1.5}\frac{\rho}{h(\kappa)\cdot f_c}\right)^2+m(h(\kappa))\left(\frac{\rho}{\sqrt{6}\cdot h(\kappa)\cdot f_c}r(\theta)+\frac{\xi}{\sqrt{3}\cdot h(\kappa)\cdot f_c}\right)-c(\kappa)=0 \qquad (1)$$

where ξ,ρ,θ are the Haigh–Westergaard coordinates of the stress tensor $\boldsymbol{\sigma}$ (bold symbols are used to denote non-scalar variables), κ is the internal state variable (ISV), f_c is the uniaxial compressive strength, m is the friction parameter determined by f_c and the spurious uniaxial tensile strength $\bar{f}_t$, r is the deviatoric shape function, and h and c are the hardening and softening variables.

The evolution of the yield surface is controlled by the variations of h and c, which are in turn driven by the accumulation of the ISV, whose rate form: $\dot{\kappa}=\sqrt{\dot{\boldsymbol{\varepsilon}}_p:\dot{\boldsymbol{\varepsilon}}_p}/\chi_p(\eta)$, where $(\dot{\ })$ indicates the rate of the variable, $\boldsymbol{\varepsilon}_p$ is the plastic strain tensor, and χ_p is a function of the confinement measure η which is defined to depend on the hydrostatic stress invariant and the deviatoric polar angle (or the Lode angle) and is thus capable of describing non-uniform confinement. The function of χ_p was obtained by generalizing the one-dimensional relationship between the active confining stress and the axial strain at peak axial stress proposed by Teng et al. (2007) and Lim and Ozbakkaloglu (2015c) into a relationship between the confinement measure η (related to the confining stress) and the total plastic strain (related to the axial strain at peak axial stress). Therefore, χ_p is independent of the specific confinement condition of the structure being modelled and can accurately predict the ductility increase of concrete under various levels of passive confinement stiffness and active confinement stress, as is revealed through the comparison between numerical predictions and experimental data in Zheng and Teng (2022a). The EPT model can potentially be used to predict the behavior of concrete confined with a single material or a combination of materials such as mild steel, high strength steel, and various types of FRPs. When there is no confinement, the confinement measure $\eta = 0$, and $\chi_p = 1$. As a result, the accumulation of the ISV becomes $\dot{\kappa} = \sqrt{\dot{\boldsymbol{\varepsilon}}_p : \dot{\boldsymbol{\varepsilon}}_p}$. When the confinement is non-zero, the confinement measure has a positive value, i.e., $\eta > 0$, and χ_p is larger than 1, and both increase with the confinement level. Accordingly, the accumulation of the ISV is slowed down, as now $\dot{\kappa} = \sqrt{\dot{\boldsymbol{\varepsilon}}_p : \dot{\boldsymbol{\varepsilon}}_p}/\chi_p$, mathematically representing the increase of ductility due to confinement. The state at which the concrete reaches the strength surface is referred to as the transition state when the critical ISV value is attained (i.e., $\kappa = \kappa_c$). In the pre-transition stage, h increases from an initial value of $0 < h_0 < 1$ to 1 (under uniaxial compression, $h \propto -\sigma_3/f_c$), and $c = 1$. In the post-transition stage, $h = 1$ and c decreases from 1 and approaches 0 asymptotically (under uniaxial compression, $c \propto -\sigma_3/f_c$), with the decreasing rate of c determined by the softening rate parameter, κ_s (a smaller κ_s value means a faster decrease of c).

The plastic strain increment is governed by the flow rule $\dot{\boldsymbol{\varepsilon}}_p = \dot{\lambda} g_\sigma$, where g_σ denotes the derivative of the potential function (g) by the stress tensor, and $\dot{\lambda}$ is the plastic multiplier. The newly proposed potential surface, having capped meridians and bulged-triangular deviatoric traces, is expressed as follows:

$$g(\xi,\rho,\theta;\kappa) = r\big(\theta,\varrho(\kappa)\big)\cdot\rho + A(\kappa)\cdot(B(\kappa)\cdot f_c - \xi)\cdot\ln\frac{B(\kappa)\cdot f_c - \xi}{\xi_0} = 0 \qquad (2)$$

where $A(\kappa)$ and $B(\kappa)$ control the shape of meridians and can be determined by the plastic Poisson's ratio (the ratio between the lateral and the axial plastic strain increments when the concrete is under compression with no or uniform confinement) at the transition state, ψ_k; $r\big(\theta,\varrho(\kappa)\big)$ controls the shape of deviatoric traces by varying the value of $\varrho(\kappa)$; ξ_0 is a constant determined by $g(\boldsymbol{\sigma};\kappa) = 0$. In the pre-transition stage, $\varrho(\kappa) = \varrho_0$ and the deviatoric trace is nearly circular; a default value of $\varrho_0 \approx 0.85$ was suggested. In the post-transition stage, $\varrho(\kappa)$ approaches ϱ_∞ and the deviatoric trace becomes increasingly more triangular; a default value of $\varrho_\infty \approx 0.6$ was suggested. The significant difference between the newly proposed potential surface and those of previous models is the evolutionary deviatoric trace that is essential for accurately predicting the dilation of concrete under multiaxial compression. Therefore, the new constitutive model may be referred to as the evolutionary potential-surface trace (EPT) model for clarity.

The EPT model has 9 material constants (parameters): the uniaxial compressive strength, f_c; the corresponding axial strain, ε_{co}; the elastic modulus, E; the Poisson's ratio, ν; the softening rate parameter, κ_s; the plastic Poisson's ratio at the transition state, ψ_k; the fictitious uniaxial tensile strength, $\bar{f_t}$; and the initial and final potential-surface deviatoric trace shape factors: ϱ_0 and ϱ_{∞}. The first group (f_c, ε_{co}, E, ν, κ_s) influences concrete behavior under all conditions and can be calibrated from uniaxial compression tests; the second group (ψ_k, $\bar{f_t}$) influences concrete behavior under confinement and can be calibrated from compression tests of concrete under either uniform or non-uniform confinement; and the last group (ϱ_0, ϱ_{∞}) influences concrete behavior only under non-uniform confinement and has to be calibrated from compression tests on concrete under non-uniform confinement. All nine parameters are treated as being independent of each other; for instance, different concretes with the same f_c value can have different values of ε_{co}, E, or ψ_k. Nevertheless, when experimental data for ε_{co},

E, ν and $\bar{f_t}$ are unavailable, their values can be estimated from f_c using empirical relationships established by previous researchers. In addition, the default values of κ_s, ψ_k, ϱ_0, ϱ_{∞}, which are independent of f_c, are provided for use in the EPT model, as detailed in Zheng and Teng (2022a). It is reiterated that the values of the parameters are the same for the same physically unique concrete and are independent of the nature/level of confinement or specimen geometry. The values of the parameters used in the present study are discussed in detail in the respective sections below.

It is well-known that concrete always exhibits strain-softening under active confinement (strain-hardening and -softening are simplified as 'hardening' and 'softening' herein, and discussed only with respect to the post-transition stage) (e.g., Samani and Attard 2014), while it can exhibit hardening, softening, and even mixed behavior under passive confinement, as shown by the existing experimental studies (e.g., Lam and Teng 2003b; Saleem et al. 2017; Shan et al. 2019). Figure 1a schematically shows a typical axial stress-strain curve of unconfined concrete as well as two typical axial stress-strain curves of the same concrete under passive confinement, one that is hardening due to a stiffer confining device and one that is softening before a rebound due to a softer confining device. It is critical to accurately predict the post-transition behavior of concrete under passive confinement, and therefore the related mathematical setup is briefly discussed, for the sake of simplicity, for concrete under uniform, passive confinement; the mathematical setup can then be readily understood for non-uniform, passive confinement. Figures 1b and 1c show the evolution of the yield surface in the pre- and post-transition stages on the Rendulic plane, where the minimum principal (axial) stress axis, the $-\sigma_3$ axis, forms an angle of 54.7° with the $-\xi$ axis, and the projections of the middle and the maximum principal (confining) stress axes coincide as the $-\sigma_1 = -\sigma_2$ axis is perpendicular to the $-\sigma_3$ axis. The yield surface reflects the frictional and the cohesive characteristics of concrete (Rudnicki and Rice 1975; Bazant 1978), with the slope being proportional to h (Figure 1b) and the intercept on the ξ axis being proportional to c (Figure 1c). Accordingly, in the pre-transition stage, the yield surface evolves from an initial yield surface to the steeper strength surface (Figure 1b), representing the increase of internal friction due to compaction while maintaining the same cohesion; in the post-transition stage, the yield surface shifts to the right along the $-\xi$ axis (Figure 1c), representing the gradual loss of cohesion due to cracking while maintaining the same friction.

The uniaxial compression stress path along the $-\sigma_3$ axis and a passively-confined compression stress path that deviates from the $-\sigma_3$ axis are both shown in Figure 1b (also see the corresponding $\sigma_3 - \varepsilon_3$ curves in Figure 1a). In the post-transition stage, the uniaxial compression stress path is softening. However, the passively-confined compression stress path starts from point o, and, if the increase of confinement and thus friction prevails over the decrease of c, will land at point p (Figure 1c) having a higher level of axial stress than point o, leading to hardening; otherwise, the stress path $o \rightarrow q$ is softening (also see the corresponding $\sigma_3 - \varepsilon_3$ curve in Figure 1a). Moreover, when cohesion is completely lost at the end of the post-transition stage ($c \approx 0$), the concrete is purely frictional and the level of axial stress is dependent on the confinement. Therefore, the concrete may still exhibit hardening behavior as long as the confining stress increases, as indicated by the stress path $d \rightarrow e$, which will appear as a ‘rebound’ of the axial stress as shown in Figure 1a. Consequently, the behavior of concrete under passive confinement is a result of the incessant competition between the increase of friction and decrease of cohesion, both deeply entangled with the dilation of concrete and the confining condition.

Implementation in FE analysis

The constitutive model was implemented with the widely used FE package ABAQUS version 2019 (Dassault Systemes 2020) through its user-defined material (UMAT) subroutine. An implicit Euler-backward algorithm has been developed as detailed in (Zeng et al. 1996), which is not repeated herein except for a few noteworthy issues discussed below. In the previous study (Zheng and Teng 2022a), the continuum tangent stiffness matrix was used as the material Jacobian (where $\partial g/\partial\boldsymbol{\sigma}$ was calculated algebraically), since the consistent tangent stiffness matrix (Simo and Taylor 1985) requires the calculation of the Hessian matrix, $\boldsymbol{H}$, of the potential function, g, with respect to the stress vector, $\boldsymbol{\sigma}_{6\times1}$, which is difficult for the EPT constitutive model with a relatively complicated potential function. In the present study, the difficulty is overcome by calculating the Hessian matrix through numerical differentiation as follows:

$$
\begin{aligned}
H_{ij} &= \frac{\partial^2 g(\boldsymbol{\sigma})}{\partial\sigma_i\partial\sigma_j} \\
&= \frac{g\left(\sigma_i+\delta\sigma,\sigma_j+\delta\sigma,\dots\right)-g\left(\sigma_i+\delta\sigma,\sigma_j-\delta\sigma,\dots\right)-g\left(\sigma_i-\delta\sigma,\sigma_j+\delta\sigma,\dots\right)+g\left(\sigma_i-\delta\sigma,\sigma_j-\delta\sigma,\dots\right)}{4\delta\sigma^2}
\end{aligned}
\tag{3}
$$

where '…' denotes the other four elements of the stress vector and $\delta\sigma$ is a small stress increment. A parametric study indicated that $\delta\sigma = 1\times10^{-5}$ MPa is a reasonable choice to achieve a sufficiently accurate $\boldsymbol{H}$ with an error below 0.001%. Therefore, the consistent tangent stiffness matrix, $\boldsymbol{D}^{ep}$, is used in the current study and the convergence performance and computational efficiency are much improved compared to the continuum tangent stiffness matrix approach of the previous study. To be compatible with the ABAQUS setup, the stress, strain, and stiffness tensors are represented by their Voigt form. Therefore, the consistent tangent stiffness matrix ($\boldsymbol{D}^{ep}_{6\times6}$) is calculated as follows:

$$
\boldsymbol{D}^{ep}_{6\times6} = \boldsymbol{R}_{6\times6} - \frac{\boldsymbol{R}_{6\times6}(g_{\boldsymbol{\sigma}})_{6\times1}(f_{\boldsymbol{\sigma}})^T_{6\times1}\boldsymbol{R}_{6\times6}}{(f_{\boldsymbol{\sigma}})^T_{6\times1}\boldsymbol{R}_{6\times6}(g_{\boldsymbol{\sigma}})_{6\times1} - f_\lambda}
\tag{4}
$$

where $f_{\boldsymbol{\sigma}} = \partial f/\partial\boldsymbol{\sigma}$ is the derivative of the yield (scalar) function by the stress vector, $\boldsymbol{\sigma}_{6\times1}$, $f_\lambda = \partial f/\partial\lambda$ is the derivative of the yield function by the plastic multiplier, λ, and $\boldsymbol{R}$ is a matrix calculated as follows:

$$
\boldsymbol{R}_{6\times6} = \left(\boldsymbol{I}_{6\times6} + \lambda\boldsymbol{D}_{6\times6}\boldsymbol{H}_{6\times6}\right)^{-1}\boldsymbol{D}_{6\times6}
\tag{5}
$$

where $\boldsymbol{I}$ is the identity matrix, $\boldsymbol{D}$ is the elastic rigidity matrix. It is noted that $\boldsymbol{H}$ is a symmetric matrix, while $\boldsymbol{D}^{ep}$ is non-symmetric for the present constitutive model. Finally, the minimum value of the softening variable c is limited to $c_{min} = 0.01$, which has only a trivial influence on the prediction while increasing the computational efficiency.

FE analysis of FRP-confined non-circular concrete columns

Selected column specimens

Since experimental data of local stress-strain behavior of concrete in FRP-confined columns are not available, the assumption is made here that the constitutive model is deemed to be reliable as long as the predicted section-average axial stress-axial strain behavior is close to the experimental data. Therefore, a comprehensive specimen pool consisting of FRP-confined square, rectangular, and elliptical plain-concrete column specimens reported by three different research groups was used to evaluate the newly developed EPT model. Additionally, to demonstrate the difference between the EPT model and the widely used AA plasticity models, a representative AA model developed by Yu et al. (2010b) incorporating the more accurate Jiang and Teng (2007) analytical model instead of the Teng et al. (2007) analytical model and using the local approximation method (i.e., method II in Yu et al. (2010b)) for confinement was also used to simulate the selected column specimens. All the concrete columns selected for FE simulation were only confined with an outer FRP jacket and tested under monotonic concentric axial compression.

Wang and Wu (2008) systematically investigated the effect of corner radius on the behavior of FRP-confined square normal-strength concrete columns by testing a large number of specimens, all of which were simulated in the present study and close agreement in the section-average axial stress-axial strain curve was found between the predictions and the experimental data. The predictions for six representative specimens covering concrete uniaxial compressive strengths of 31.0 and 53.0 MPa and four corner radii are presented herein to evaluate the EPT model and investigate the effect of corner radius on the local concrete behavior in square columns.

In a study conducted by Ozbakkaloglu (2013), the behavior of FRP-confined rectangular high-strength concrete columns, covering the two corner radii of 15 and 30 mm, was investigated. Since the effect of corner radius was the focus of the simulations of the square columns, the simulations of the rectangular columns were placed on the effect of section aspect ratio. Only columns with a 15 mm corner radius were thus selected for the simulations, and these columns were chosen instead of those with a 30 mm corner radius as the former exhibit more significant non-uniformity than the latter. Therefore, a total of six specimen configurations (each having two nominally identical specimens) covering aspect ratios of 1, 1.5, and 2 and two levels of FRP confinement were simulated to evaluate the EPT model and investigate the effect of aspect ratio on the local concrete behavior in rectangular columns.

Elliptical sections were the third non-circular section form considered in the numerical simulations. Available experimental results of FRP-confined elliptical concrete columns are rather limited (Teng and Lam 2002; Teng et al. 2016;), and the experimental work recently reported by the authors' research group (Liu et al. 2022) provided the most comprehensive experimental data for FRP-confined elliptical columns. A total of 16 columns with filament-wound FRP tubes having fibers close to the hoop direction (so that their axial stiffness can be neglected in the numerical simulations) were tested, covering two levels of FRP confinement, three concrete strengths, and four section aspect ratios. Since the selected square columns included two concrete strengths and the selected rectangular columns included two FRP confinement levels, only four elliptical normal-strength concrete columns covering the aspect ratios of 1, 1.5, 2, and 2.5 were simulated to evaluate the EPT model and investigate the local behavior of concrete in elliptical columns. For convenient reference to the specimens, they are assigned new names indicating sequentially their cross-sectional shape ('S' for square, 'R' for rectangular, and ‘E’ for elliptical), aspect ratio, corner radius (denoted by ‘r’), number of FRP layers (denoted by ‘L’), and uniaxial compressive strength of concrete; identical features within the group are not reflected in the names. The details of the specimens, including their original names, are summarized in Table 1.

FE models

A slice model was used to simulate the selected columns based on the assumption that the effect of the column-end constraints on the section-average behavior at the mid-height section (or the mid-height region) is negligible (Teng et al. 2015b); the thickness of the slice was taken as 10 mm. Since all specimens had a doubly-symmetric cross-section, a quarter model was adopted. The monotonic concentric compression imposed on the column was simulated by applying a uniform axial displacement over the section. The concrete was simulated using 8-node brick elements with reduced integration and enhanced hourglass control, the FRP jacket was simulated using 4-node membrane elements with reduced integration, and the FRP-to-concrete interface was simulated as a perfect bond. A mesh convergence study indicated that an element size of 5 mm within the section was sufficient as reducing the element size further was found to lead to indistinguishable changes to the predicted section-average axial stress-axial strain responses.

The material behavior of concrete was simulated using both the newly developed EPT model (Zheng and Teng 2022a) and the AA model (Yu et al. 2010a) that incorporates the more accurate core analytical model developed by Jiang and Teng (2007) instead of the Teng et al. (2007) model. The AA model requires tabulated input data generated using four input parameters: f_c, ε_{co}, E, and ν. The determination of parameter values is detailed in the discussions below for each group of specimens. The FRP jacket was simulated as an orthotropic linear elastic material with the major principal stress direction being the hoop direction of the column section, while the modulus in the axial direction of the column was assigned the small value of 0.1 GPa. The rupture strain of the FRP jacket was taken as 1.5%, which is around the measured maximum FRP hoop strain in Wang and Wu (2008) and Liu et al. (2022) and the ultimate tensile strain from FRP coupon tests in Ozbakkaloglu (2013), to allow for the development of sufficient concrete dilation as the focus of the present study is to understand the local behavior of concrete over a realistically wide range of deformation levels.

Square columns

For the selected square columns, Wang and Wu (2008) reported the axial stress-axial strain and axial stress-hoop strain curves of six columns, with each of these columns being selected from three nominally identical columns for one of the six column configurations. They also reported the results of six corresponding unconfined concrete columns, with each of these six unconfined columns being also selected from three normally identical specimens. The values of E, f_c, and ε_{co} were obtained as their averages of the six axial stress-axial strain curves of the unconfined columns. Moreover, the value of κ_s was calibrated by matching the descending branches of the predicted axial stress-axial strain curves with the descending branches of the six experimental axial stress-axial strain curves. Parameters ψ_k and $\bar{f_t}$ were calibrated by matching the predicted axial stress-axial strain curve of the FRP-confined circular column (i.e., the square column with a maximum corner radius of 75 mm) with the reported curve. As discussed above, these two parameters can be calibrated using the test data of any confined concrete column (in this case the circular column) and then used for predicting the behavior of the square columns. Therefore, the values of the parameters are specific to the concrete material, but the EPT model is not limited to any specific condition of FRP confinement. The default values of $\varrho_0 = 0.85$ and $\varrho_\infty = 0.6$ were used, and a typical value for ν, namely 0.18, was assumed. The values of the parameters for the EPT model are summarized in Table 2. The values of E, f_c, ν, and ε_{co} used in the AA model are the same as those in the EPT model. The values of elastic modulus and nominal layer thickness of the FRP jacket as reported by the authors, being 220 GPa and 0.165 mm respectively, were adopted in the simulations.

The average axial stress-axial strain and axial stress-hoop FRP strain (averaged from two opposite mid-side locations in the experiment) curves of the six specimens predicted with the EPT and the AA models are compared with the experimental data extracted from the study of Wang and Wu (2008) in Figure 2. To make the discussions simpler and consistent with the conventional definition that compressive stresses are taken as positive stresses in concrete, compressive stresses are presented as positive values (i.e., referring to stresses using the $-\sigma$ values) from here onwards. Specimens Sr0L1C31, Sr0L2C53, and Sr15L1C31with sharp corners or a relatively small corner radius, as shown in Figures 2a, 2b, and 2c, respectively, exhibit a softening behavior. For specimens Sr15L2C53 and Sr30L2C53 with a larger corner radius, as shown in Figures 2d and 2e, respectively, a hardening response following the softening branch can be seen. The predictions for these five specimens obtained with the EPT model successfully capture the behavior and are close to the experimental data, but those obtained with the AA model are incapable of predicting the strongly softening behavior for these square sections. For specimen S1r60L2C53 with a nearly circular section, both models predict a hardening second branch that closely matches the experimental data, as shown in Figure 2f. Figure 2 therefore demonstrates that the EPT model is accurate for FRP-confined square concrete columns with any corner radius, while the AA model is only suitable for those with a large corner radius. In addition, the default parameter values based only on f_c are summarized in Table 5. Although it is unnecessary to use the default values of ε_{co} and E when they are available, the use of the default values for all parameters is considered herein for comparison purposes; predictions using these default values were obtained for Sr15L1C31 and Sr15L2C53. The results are shown as the dashed blue curves in Figures 2c and 2d. It is seen that the post-peak softening nature of the behavior of the specimens can still be predicted, although the predictions are much less accurate due to the use of less accurate parameter values.

Four states along the loading process representing the pre-damage (the concrete over the entire section is in the pre-transition stage), early damage (the concrete somewhere in the section has entered the post-transition stage and is considered 'damaged'), moderate damage (more concrete has entered the post-transition stage), and severe damage (the concrete somewhere in the section has lost its cohesion and is considered 'completely damaged') states of the concrete are indicated by the four points A, B, C, and D on the stress-strain curves predicted with the EPT model; the severely damaged state D is also indicated for the AA predictions. The local concrete stresses at these states predicted by the models are examined below.

The axial stress distributions predicted with the EPT constitutive model from a quarter FE model for the four C53 columns with corner radii of 0, 15, 30, and 60 mm are visualized over the entire section as 3D surfaces as shown in Figures 3, 4, 5, and 6 for the four states, respectively. In each plot, the two horizontal axes define the location within the section, and the vertical axis indicates the magnitude of axial compressive stress. To clearly identify the distribution of effectively-confined concrete within the section, the level of f_c is indicated in each plot as the grey plane, and the level of 5% higher than f_c, i.e., 1.05 f_c, is indicated as the dashed contour on the 3D stress-distribution surface. The corresponding boundaries of the regions above these two stress levels are projected as solid (f_c) and dashed (1.05 f_c) curves on the cross-section shown below the 3D stress distribution. In the present study, the regions where the concrete stress is above the 1.05 f_c level is referred to as the effective-confinement areas (ECAs), and the remaining regions are referred to as the under-confinement areas (UCAs).

At the pre-damage state A (Figure 3), in all four sections, the axial stress over the whole section is slightly above the f_c level and barely non-uniform since the confinement provided by FRP is small. At the early damage state B (Figure 4), in the sharp-corner section (r = 0), high stresses are observed in the central region, forming a central plateau, and low stresses are seen in the corner regions; the ECA is a square-shaped central region. By contrast, in the other three sections which have rounded corners, the highest stresses are found near the corners while the lowest stresses are seen near the edges; the ECA exhibits the typical arching-effect pattern and its size is larger for a larger corner radius. Compared with the stress distribution at state A, the axial stress at state B becomes higher in the ECA but much lower in the UCA/UCAs (referred to only as UCAs in general for simplicity), resulting in a sharp increase of non-uniformity. With further loading to state C (Figure 5), the total area of ECA/ECAs (referred to only as ECAs in general for simplicity), decreases in all sections. Meanwhile, the stress continues to increase in the ECAs and decrease in the UCAs.

Finally, at state D (Figure 6), the ECAs in all sections are similar to those at state C, indicating that a somewhat stable ECA distribution has been reached at state C. The axial stress distributions predicted with the AA model at state D are compared with the EPT predictions in Figure 6; they are very different from each other except for the 60-mm corner radius section. The AA model predicts a much larger total ECA size and a much higher stress level in the UCAs than the EPT model. Hence, the AA model was unable to predict the strongly softening behavior seen in the experimental data. Indeed, the patterns of the state-D AA predictions are generally close to those of the state-B EPT predictions (Figure 4) for round-corner sections, implying that a considerable evolution process of local concrete stresses was missed by the AA model. The EPT predictions indicate that the total size of ECAs continuously decreases along the loading process until reaching stabilization at a late stage, as can be seen by comparing Figures 3-6. This is because the EPT model predicts strain-softening behavior for concrete under highly non-uniform confinement, and therefore the total size of ECAs decreases as the axial stress of concrete in the ECAs drops below the $1.05f_c$ level. This is contrary to the findings in Lin and Teng (2020) based on the FE predictions made with the same AA model, which indicate that the total ECA size continuously increases along the loading process. As a result, the present study based on the predictions with the EPT model depicts a much smaller total ECA size than that observed by Lin and Teng (2020).

The results of local principal confining stresses (i.e., σ_1 and σ_2) indicate that their directions are basically unchanged throughout the loading process for square columns. Figure 7a shows the typical directions and relative magnitudes of σ_1 and σ_2 for the 0- and the 15-mm corner radius sections. Obviously, the concrete at the center is under equal lateral stresses (i.e., uniform confinement), and the concrete in a small area around the center is under nearly equal principal confining stresses ($\sigma_2/\sigma_1 \approx 1$), i.e., nearly uniform confinement; the confining-stress non-uniformity (σ_2/σ_1) increases as the location moves away from the center, as can be seen that $\sigma_1 \approx 0$ near the edges and $-\sigma_2 \gg -\sigma_1$ in the corner regions. Namely, the concrete in most parts of the section is subjected to highly non-uniform confinement. Similar observations of the local principal confining stress directions and the distribution of confining-stress non-uniformity were made by Lin and Teng (2020). The local axial stress-axial strain curves for concrete along the center-to-corner, center-to-edge, and corner-to-edge paths are shown in Figure 7b for the two sections; a higher axial stress level indicates more effective confinement. Therefore, for the sharp-corner section, the levels of confinement are ranked from high to low as: center, edge, corner; for the rounded corner section: corner, center, edge. Obviously, the FRP provides very high confinement to concrete in the rounded corner regions, but the confinement is very low in the vicinities of the sharp corners. It is noted that, although the confinement in the rounded corner regions is the highest, it is highly non-uniform with a very high level of σ_2. Moreover, the local axial stress-strain curves in all UCAs exhibit an initial rapidly softening behavior until complete damage (corresponding to point *d* in Figures 1a and 1c, where $c = 0$), which is followed by a rebound of the axial stress (corresponding to point *e* in Figures 1a and 1c, where confinement is slightly increased). It should be noted that as a quarter model was used in all the simulations and the stresses and strains at the Gauss integration points are used, the ‘center’, ‘edge’ and ‘corner’ locations indicated in the figure are not exactly the geometric center, mid-edge point, and corner point but are the Gauss integration points nearest to them respectively. The same applies to the results for the rectangular and the elliptical columns, as discussed in Figures 11 and 14. This location approximation does not compromise the observations and discussions of local stress-strain behavior in the sections.

By considering the details presented above, the behavior of a square concrete column confined with FRP and subjected to monotonic concentric compression can be explained as follows. Before the concrete enters the post-transition stage, the entire section can be considered as an ECA, with relatively low levels of confinement near the flat sides. With further loading, the concrete near the flat sides is damaged rapidly and exhibits softening behavior due to the low levels of confinement there; therefore, these regions become UCAs. With continuous loading, the ECAs shrink while the UCAs propagate. Meanwhile, the confinement in the ECAs increases and the shrinking process slows down continuously because the decohesion process of concrete in the ECAs becomes slower. Eventually, a balance between the ECAs and the UCAs is achieved in this dynamic process, and by then, the concrete in the UCAs has been completely damaged. Generally, during this stable stage, a square-shaped central ECA exists regardless of the corner radius, but the size of the ECAs near the corners is proportional to the corner radius. Accordingly, the central ECA dominates the confinement behavior for small-corner-radius sections, and the ECAs in the vicinities of the center and the corners merge into the arching-effect pattern for large-corner-radius sections.

Rectangular columns

The rectangular high-strength concrete columns had a reported average uniaxial compressive cylinder strength of 77.9 MPa (Ozbakkaloglu 2013), which was used as f_c in the FE simulations. Since ε_{co} and E were not reported, they were taken as the averages of values measured from the axial stress-axial strain curves of the FRP-confined rectangular column specimens. The influence of confinement should be negligible on E but could be non-trivial on ε_{co}. The value of ε_{co} was thus taken as the average of ε_{co} values of the two nominally identical specimens denoted by R2L3 as these were the least-confined specimens (i.e., with the highest aspect ratio and lowest FRP confinement level). Parameters ψ_k, $\bar{f}_t$, and κ_s were determined by matching the FE results with the experimental data of the square column specimens R1L3 (two nominally identical specimens). The default values of $\varrho_0 = 0.85$ and $\varrho_\infty = 0.6$ were used, and a typical value of $\nu = 0.18$ was assumed. The values of the parameters in the EPT model are summarized in Table 3. The values of f_c and ε_{co} used in the AA model are the same as those in the EPT model. Unlike the EPT model, however, the AA model requires a sufficiently large value of $(E\varepsilon_{co})/f_c$. The values of E, f_c and ε_{co} obtained from the test data, $(E\varepsilon_{co})/f_c = 1.4$, do not meet this requirement and lead to convergence problems with the AA model. By adopting the measured values of $f_c = 77.9$ and $\varepsilon_{co} = 0.0034$, the minimum admissible value of E by the AA model was found to be 45,900 MPa, which was used in the AA model for the predictions. This use of a revised value for the elastic modulus, together with the original values of f_c and ε_{co}, has only a rather small overall effect on the predicted axial stress-strain curve, with a greater effect on the ascending branch than the descending branch of the curve. The values of elastic modulus and layer thickness of the FRP jacket as reported by the authors, being 240 GPa and 0.234 mm respectively, were adopted in the simulations.

The average axial stress-axial strain curves predicted with the EPT and the AA models are compared with the experimental data of 3- and 5-layer FRP-confined specimens (a total of six configurations, each having two nominally identical specimens) extracted from the study conducted by Ozbakkaloglu (2013) in Figures 8a and 8b, respectively. All specimens show a three-branch behavior including an initial pre-damage branch, then a softening branch, and finally a slowly hardening branch. Such behavior has also been reported for rectangular columns under concentric compression in other studies (e.g., Lam and Teng 2003b; Ozbakkaloglu and Oehlers 2008; Wu and Wei 2010; Saleem et al. 2017). For specimens with the same number of FRP layers, a higher aspect ratio leads to a steeper softening branch and a lower stress level for the hardening branch. The predictions obtained with the EPT model successfully capture this overall trend for all specimens and are close to the experimental data. In addition, predictions for R1L3 with the EPT model were made using the default parameter values given in Table 5. It is noted that the default value of E is 41,700 MPa, which is much larger than the measured value of E. The results are shown as the dashed blue curve in Figure 8a; it is seen that the predictions still indicate a softening behavior of the specimen during the initial post-peak stage, although the stresses are substantially over-predicted.

By contrast, the AA model was unable to predict the softening behavior of the rectangular columns even for the one with an aspect ratio of 2. Indeed, the AA predictions for rectangular columns with different aspect ratios are similar, which indicates that the AA model is inaccurate for FRP-confined rectangular concrete columns. Similarly, the four states representing the increasing levels of damage for the concrete column are marked on the stress-strain curves predicted with the EPT model, and the final state D for the AA predictions is also marked. The predicted local responses of concrete at these states are examined below.

The 3D axial stress distributions predicted with the EPT model for the two rectangular columns confined with 3 layers of FRP are given in Figure 9 for the first three states and in Figure 10 for the last state. At the pre-damage state A, the axial stresses over the two sections are slightly higher than f_c and basically uniform. At the early damage state B, the ECAs in both sections exhibit the typical arching-effect pattern. At state C, the ECAs in both sections have shrunk substantially, leaving separate ECAs around the two focal points (referred to as side-centers and indicated as c_s in the figure) with a nearly triangular shape and near the corners. The stresses adjacent to the long-side edge (e_L) are the smallest within the section. With further loading to state D (Figure 10), for both sections, the ECAs are similar to those at state C, indicating that stable ECAs have been reached at state C. The axial stress distributions at state D predicted with the AA model are also given in Figure 10, which are very different from those predicted with the EPT model for both sections. Similar to the predictions for the square sections, the AA model leads to a much larger total ECA size (almost the entire section in this case) and a much higher stress level in the UCAs than the EPT model. The ECA distributions at state D predicted with the AA model are somewhat similar to those at state A predicted with the EPT model, indicating the process of local concrete evolution is not well captured by the AA model.

Figure 11a shows the typical directions and relative magnitudes of σ_1 and σ_2 for both rectangular sections. Generally, the concrete in a small area around each side-center is subjected to nearly equal principal confining stresses ($\sigma_1/\sigma_2 \approx 1$), and the confinement non-uniformity (σ_2/σ_1) increases as the location is further away from the side-centers; $\sigma_1 \approx 0$ near e_L and e_B and $-\sigma_2 \gg -\sigma_1$ near the corners. The concrete in most parts of the section is subjected to highly non-uniform confinement. The local axial stress-axial strain responses at the corners, the side-centers, the geometric center (c_g), and the two edges are shown in Figure 11b for both sections. Obviously, the confinement is the most effective near the rounded corners for both sections, and is the second most effective in small areas around the side-centers, where the concrete is nearly uniformly confined. The confinement is less effective around the geometric center than that around the two side-centers. Near the two edges, the concrete exhibits rapid softening behavior followed by a slowly softening or hardening branch, as a result of the low confinement there.

By comparing the local responses of concrete in square and rectangular sections, it is evident that the concrete around the center of square sections and the concrete around the side-centers of rectangular sections behave similarly; and the same can be said about the concrete adjacent to the rounded corners of square and rectangular sections as well as about the concrete in the UCAs of square and rectangular sections. The only obvious difference is that the ECAs around the side-centers of rectangular sections are triangular-shaped, while that around the center of square columns is square-shaped. Consequently, the local behavior of concrete in a rectangular section can be understood by referring to that in a square section, as discussed above.

Elliptical columns

For the group of elliptical specimens considered in the present study, the values of f_c, ε_{co}, E, and ν of the concrete were reported by Liu et al. (2022); they were obtained from compression tests of concrete cylinders with a diameter of 150 mm and a height of 300 mm. The value of κ_s was determined by matching the predictions of the descending branch with the test data of the cylinders. Parameters ψ_k and $\bar{f}_t$ were determined by matching the predictions with the test data of the FRP-confined circular column E1. The default values of $\varrho_0 = 0.85$ and $\varrho_\infty = 0.6$ were used. The values of the parameters used for the EPT model are summarized in Table 4. The values of f_c, ε_{co}, E and ν used in the AA model are the same as those in the EPT model. The elastic modulus and thickness of the FRP jacket were 38.1 GPa and 3.3 mm respectively, as reported by the authors.

The section-average axial stress-axial strain curves predicted with the EPT and the AA models are compared with the experimental data of Liu et al. (2022) in Figures 12a and 12b, respectively. Column E2.5 exhibits an initial softening behavior followed by a hardening branch similar to the behavior of rectangular columns, which is successfully captured by the EPT predictions. Column E2 shows a slowly hardening behavior, and the predictions obtained with the EPT model are close to the experimental data. For columns E1.5 and E1, the experimental data show hardening behavior that was closely predicted with the EPT model. In addition, predictions with the EPT model for column E2 were made using the default parameter values given in Table 5. The default values are close to the calibrated values of the parameters, and the predictions, shown as the dashed red curve in Figure 12a, are close to the experimental data of E2.

By contrast, the AA model was unable to predict the softening behavior of E2.5 or the slightly hardening behavior of E2. Indeed, the stress-strain curves predicted with the AA model for the four elliptical columns are quite close, which indicates the unsuitability of the AA model for FRP-confined elliptical columns with large aspect ratios. The four states of interest are indicated in the charts.

The axial stress distributions for the four sections at state D predicted with both models are compared in Figure 13. The stress distributions at state D of the E1 and the E1.5 sections predicted with the two models are similar; the axial stresses over the entire section exceed the $1.05f_c$ level (the dashed contour line indicating the $1.05f_c$ level is absent because the entire stress surface is above the $1.05f_c$ level). However, for the E2 and the E2.5 sections, the EPT model predicts ECAs adjacent to the vertices (i.e., the ends of the major axis) separated by a UCA in the central region, while the AA model still predicts that the axial stresses over the entire section exceed the $1.05f_c$ level. As a result, the AA model was unable to predict the slowly hardening behavior of E2 and the softening behavior of E2.5.

The local principal confining stresses for E1.5 and E2.5 are presented in Figure 14a. In both sections, the confinement is nearly uniform ($\sigma_1 \approx \sigma_2$) in a small area near each vertex, and the confinement non-uniformity (σ_2/σ_1) increases as the location is further away from the vertices. For column E1.5, the non-uniformity is rather moderate as σ_1 is non-trivial around the center and near the co-vertices (i.e., ends of the minor axis). By contrast, for column E2.5 having a much larger aspect ratio, the confinement is highly non-uniform both around the center and near the co-vertices: where $\sigma_1 \approx 0$. Consequently, as shown in Figure 14b, the local axial stress-axial strain response is hardening at the vertices for both elliptical sections, but it is hardening around the center and at the co-vertices for E1.5 while softening for E2.5. Similar to the local concrete behavior in the UCAs of square and rectangular sections, the local softening behavior gradually becomes slightly hardening as concrete approaches the complete damage stage, corresponding to the stress path between points *d* and *e* in Figure 1. Accordingly, at the section level, the average axial stress-axial strain response becomes slightly hardening eventually.

By comparing the local behavior of concrete in elliptical sections with that in square and rectangular sections, it can be readily seen that the behavior of concrete near the vertices of an elliptical section is akin to that around the center of a square section and the side-centers of a rectangular section, and the behavior of concrete in the UCAs in all non-circular columns is similar. Specifically, in terms of local concrete behavior, there is no region in an elliptical section that resembles the rounded corner regions in a square or rectangular section. The total size of ECAs as a proportion of an elliptical section decreases as the aspect ratio increases.

Direct measurement of local axial stress

The authors' group has previously made an attempt to experimentally measure local axial stresses in a series of FRP-confined square and rectangular columns, of which one rectangular column was reported in a conference paper (Teng et al. 2015a). In that study, an FRP-confined concrete column specimen was prepared as two nominally identical halves. During the concentric compression loading process, a thin film containing a 2D array of piezoelectric sensors (referred to as the pressure mapping system) was placed between the two halves (i.e., at the mid-height section of the test specimen) to measure the local axial stresses. Considering the unevenness of the concrete surfaces sandwiching the pressure film, the random coarse aggregate distribution, and the possible calibration errors of the pressure mapping system, among other uncertainties, the accurate measurement of local stresses in these test specimens and their robust interpretation is no small challenge. Furthermore, Teng et al. (2015a) presents only the local axial stresses measured in one of the test columns and their comparisons with FE predictions obtained with the AA model. During the present study, significant discrepancies between the present AA predictions and those given in Teng et al. (2015a) were found, suggesting that the FE results in Teng et al. (2015a) have involved some important errors. Due to the above reasons, it is difficult to reach a firm conclusion on the accuracy of FE predictions through comparison with the test data in Teng et al. (2015a). Nevertheless, a new attempt of comparing the test data for the chosen column specimen reported in Teng et al. (2015a) and the newly obtained predictions with the EPT and the AA models are presented in Appendix A for additional reference.

Conclusions

In the present paper, an FE study of FRP-confined square, rectangular, and elliptical columns under monotonic concentric compression has been reported. The FE analysis is based on the EPT (evolutionary potential-surface trace) plasticity constitutive model for concrete recently proposed by the authors and reported in a previous paper (Zheng and Teng 2022a). The key components of the model have been briefly introduced, and its implementation with the FE package ABAQUS through an Euler-backward algorithm employing the consistent tangent matrix has been explained. It has also been demonstrated that the model provides accurate predictions of the section-average behavior for all the selected FRP-confined non-circular plain-concrete columns. Therefore, the FE predictions for the local behavior of concrete were deemed to be closely reflective of the real local behavior of concrete. Based on the FE results, the following conclusions can be made for FRP-confined non-circular concrete columns under axial compression:

i. In all non-circular sections, the confinement to concrete is significantly non-uniform except in the close vicinities of the center of a square section, the two side-centers of a rectangular section, and the two vertices (ends of the major axis) of an elliptical section, where the concrete is under nearly uniform confinement. In much larger areas surrounding these small areas of nearly uniform confinement, the concrete is effectively confined, as indicated by having axial stresses exceeding $1.05 f_c$; these larger areas are referred to as effective-confinement areas (ECAs).

ii. For square and rectangular sections with rounded corners, the confinement in the rounded corner regions is more effective, although highly non-uniform, than that in the other ECAs surrounding the center or side-centers. Hence, the rounded corner regions also qualify as ECAs.

iii. When the concrete somewhere in the section enters the softening stage or starts to experience damage, the ECAs shrink continuously but at a reducing rate of shrinkage as the deformation level increases, with associated changes in the shapes of ECAs. Meanwhile, the level of confinement in the ECAs continuously increases. Eventually, as a result of these two dynamic processes, a nearly stable ECA distribution in the section is reached. Generally, around the center of a square section, the ECA has a square shape, and around the side-centers of a rectangular section, the ECAs have a triangular shape; their shapes and sizes are little influenced by the corner radius. Near the corners of a square or a rectangular section, the size of the ECAs is related to the corner radius, and near the vertices of an elliptical column, the size of the ECAs is adversely proportional to the section aspect ratio.

iv. The concrete in the ECAs generally exhibits either a hardening or a slowly softening stress-strain response and suffers only moderate damage even at a late stage of loading. The concrete in the remaining regions (under-confinement areas or UCAs) generally exhibits a rapidly softening response until it is completely damaged, and thereafter it exhibits a slowly hardening response.

v. The section-average axial stress-axial strain behavior of an FRP-confined non-circular concrete section is an outcome of the interplay between the ECAs and the UCAs. The average behavior appears as hardening if the effect of the ECAs dominates and softening otherwise. Notably, the effect of the ECAs seems to be more dependent on the geometric parameters of the section, including the section shape, aspect ratio and corner radius, than the stiffness of the FRP confining jacket/tube.

The EPT plasticity constitutive model can potentially be used to gain a deeper understanding of confinement mechanisms and obtain numerical results for the establishment of more accurate analytical models for the section-average stress-strain behavior of FRP-confined non-circular concrete columns. The EPT model can also be used in three-dimensional FE models for predicting the behavior of concrete columns with more complicated forms of confinement, but it should be noted that such FE models are likely to be subject to mesh-dependence when strain-softening behavior is involved. The EPT plasticity model summarized in the present paper enriched with non-local features will be presented in a forthcoming paper to address the mesh-dependence issues.

Data Availability Statement

Some data and the computer code that support the findings of this study are available from the corresponding author upon reasonable request. The available data include the results of the finite element analyses. The mathematical formulation of the adopted plasticity model for concrete is available at https://doi.org/10.1016/j.engstruct.2021.113435, and its FORTRAN code may be released by the authors in the future.

Acknowledgment

The authors are grateful for the financial support received from the Research Grants Council (RGC) of the Hong Kong Special Administrative Region, China (Project Nos.: PolyU152203/18E and T22-502/18-R).

References

Bazant, Z. P. 1978. "Endochronic inelasticity and incremental plasticity." Int. J. Solids Struct., 14 (9): 691–714. https://doi.org/10.1016/0020-7683(78)90029-X.

Dassault Systemes. 2020. "ABAQUS: Theory and User's manuals."

Doran, B., H. O. Koksal, and T. Turgay. 2009. "Nonlinear finite element modeling of rectangular/square concrete columns confined with FRP." Mater. Des., 30 (8): 3066–3075. https://doi.org/10.1016/j.matdes.2008.12.007.

Ekop, I., and P. Grassl. 2022. "On finite element modelling of concrete columns with non-circular cross-sections confined with carbon fibre reinforced polymer." In: UK Association for Computational Mechanics (UKACM) Conference 2022, Nottingham, UK.

Fanaradelli, T. D., and T. C. Rousakis. 2020. "3D Finite Element Pseudodynamic Analysis of Deficient RC Rectangular Columns Confined with Fiber Reinforced Polymers under Axial Compression." Polymers, 12 (11): 2546. https://doi.org/10.3390/polym12112546.

Grassl, P., K. Lundgren, and K. Gylltoft. 2002. "Concrete in compression: A plasticity theory with a novel hardening law." Int. J. Solids Struct., 39 (20): 5205–5223. https://doi.org/10.1016/S0020-7683(02)00408-0.

Hajsadeghi, M., F. J. Alaee, and A. Shahmohammadi. 2011. "Investigation on behaviour of square/rectangular reinforced concrete columns retrofitted with FRP jacket." J. Civ. Eng. Manag., 17 (3): 400–408. https://doi.org/10.3846/13923730.2011.594155.

Han, D. J., and W. F. Chen. 1985. "A nonuniform hardening plasticity model for concrete materials." Mech. Mater., 4 (3–4): 283–302. https://doi.org/10.1016/0167-6636(85)90025-0.

Hany, N. F., E. G. Hantouche, and M. H. Harajli. 2016. "Finite element modeling of FRP-confined concrete using modified concrete damaged plasticity." Eng. Struct., 125: 1–14. Elsevier Ltd. https://doi.org/10.1016/j.engstruct.2016.06.047.

Jiang, J.F., and Y.F. Wu. 2012. "Identification of material parameters for Drucker–Prager plasticity model for FRP confined circular concrete columns." Int. J. Solids Struct., 49 (3–4): 445–456. https://doi.org/10.1016/j.ijsolstr.2011.10.002.

Jiang, J.F., P.C. Xiao, and B.B. Li. 2017. “True-triaxial compressive behaviour of concrete under passive confinement.” Constr. Build. Mater., 156: 584–598. https://doi.org/10.1016/j.conbuildmat.2017.08.143.

Jiang, T., and J. G. Teng. 2007. “Analysis-oriented stress-strain models for FRP-confined concrete.” Eng. Struct., 29 (11): 2968–2986. https://doi.org/10.1016/j.engstruct.2007.01.010.

Karabinis, A. I., and T. C. Rousakis. 2002. “Concrete confined by FRP material: A plasticity approach.” Eng. Struct., 24 (7): 923–932. https://doi.org/10.1016/S0141-0296(02)00011-1.

Lam, L., and J. G. Teng. 2003a. “Design-oriented stress–strain model for FRP-confined concrete.” Constr. Build. Mater., 17 (6–7): 471–489. https://doi.org/10.1016/S0950-0618(03)00045-X.

Lam, L., and J. G. Teng. 2003b. “Design-oriented Stress – Strain Model for FRP-confined Concrete in Rectangular Columns.” J. Reinf. Plast. Compos., 22 (13). https://doi.org/10.1177/073168403035429.

Lam, L., and J. G. Teng. 2004. “Ultimate Condition of Fiber Reinforced Polymer-Confined Concrete.” J. Compos. Constr., 8 (6): 539–548. https://doi.org/10.1061/(asce)1090-0268(2004)8:6(539).

Lam, L., J. G. Teng, C. H. Cheung, and Y. Xiao. 2006. “FRP-confined concrete under axial cyclic compression.” Cem. Concr. Compos., 28 (10): 949–958. https://doi.org/10.1016/j.cemconcomp.2006.07.007.

Lee, J., and G. L. Fenves. 1998. “Plastic-Damage Model for Cyclic Loading of Concrete Structures.” J. Eng. Mech., 124 (8): 892–900. https://doi.org/10.1061/(ASCE)0733-9399(1998)124:8(892).

Li, B., J. Jiang, H. Xiong, Y. Zhan, Z. Wu, and L. S. Cunningham. 2021. “Improved concrete plastic-damage model for FRP-confined concrete based on true tri-axial experiment.” Compos. Struct., 269: 114051. https://doi.org/10.1016/j.compstruct.2021.114051.

Lim, J. C., and T. Ozbakkaloglu. 2015a. “Unified Stress-Strain Model for FRP and Actively Confined Normal-Strength and High-Strength Concrete.” J. Compos. Constr., 19 (4): 04014072. https://doi.org/10.1061/(ASCE)CC.1943-5614.0000536.

Lim, J. C., and T. Ozbakkaloglu. 2015b. “Investigation of the Influence of the Application Path of Confining Pressure: Tests on Actively Confined and FRP-Confined Concretes.” J. Struct. Eng., 141 (8): 04014203. https://doi.org/10.1061/(ASCE)ST.1943-541X.0001177.

Lim, J. C., and T. Ozbakkaloglu. 2015c. “Lateral Strain-to-Axial Strain Relationship of Confined Concrete.” J. Struct. Eng., 141 (5): 04014141. https://doi.org/10.1061/(ASCE)ST.1943-541X.0001094.

Lin, G., and J. G. Teng. 2017. “Three-Dimensional Finite-Element Analysis of FRP-Confined Circular Concrete Columns under Eccentric Loading.” J. Compos. Constr., 21 (4): 04017003. https://doi.org/10.1061/(asce)cc.1943-5614.0000772.

Lin, G., and J. G. Teng. 2020. “Advanced stress-strain model for FRP-confined concrete in square columns.” Compos. Part B Eng., 197: 108149. https://doi.org/10.1016/j.compositesb.2020.108149.

Liu, K.C., C. Jiang, T. Yu, and J.G. Teng. 2022. “Axial compressive behavior of elliptical FRP tube-confined concrete columns.” (Under preparation)

Lubliner, J., J. Oliver, S. Oller, and E. Oñate. 1989. “A plastic-damage model for concrete.” Int. J. Solids Struct., 25 (3): 299–326. https://doi.org/10.1016/0020-7683(89)90050-4.

Mander, J. B., M. J. N. Priestley, and R. Park. 1988. "Theoretical Stress‐Strain Model for Confined Concrete." J. Struct. Eng., 114 (8): 1804–1826. https://doi.org/10.1061/(ASCE)0733-9445(1988)114:8(1804).

Mazzucco, G., V. A. Salomoni, C. E. Majorana, C. Pellegrino, and C. Ceccato. 2016. “Numerical investigation of concrete columns with external FRP jackets subjected to axial loads.” Constr. Build. Mater., 111: 590–599. https://doi.org/10.1016/j.conbuildmat.2016.02.050.

Menetrey, P., and K. J. Willam. 1995. “Triaxial Failure Criterion for Concrete and its Generalization.” ACI Struct. J., 92 (3): 311–318. https://doi.org/10.14359/1132.

Mirmiran, A., and M. Shahawy. 1997. “Behavior of Concrete Columns Confined by Fiber Composites.” J. Struct. Eng., 123 (5): 583–590. https://doi.org/10.1061/(ASCE)0733-9445(1997)123:5(583).

Mirmiran, A., M. Shahawy, M. Samaan, H. El Echary, J. C. Mastrapa, and O. Pico. 1998. “Effect of Column Parameters on FRP-Confined Concrete.” J. Compos. Constr., 2 (4): 175–185. https://doi.org/10.1061/(ASCE)1090-0268(1998)2:4(175).

Mirmiran, A., K. Zagers, and W. Yuan. 2000. “Nonlinear finite element modeling of concrete confined by fiber composites.” Finite Elem. Anal. Des., 35 (1): 79–96. https://doi.org/10.1016/S0168-874X(99)00056-6.

Mohammadi, M., J.G. Dai, Y.F. Wu, and Y.L. Bai. 2019. “Development of extended Drucker–Prager model for non-uniform FRP-confined concrete based on triaxial tests.” Constr. Build. Mater., 224: 1–18. https://doi.org/10.1016/j.conbuildmat.2019.07.061.

Mohammadi, M., and Y.F. Wu. 2017. “Triaxial test for concrete under non-uniform passive confinement.” Constr. Build. Mater., 138: 455–468. Elsevier Ltd. https://doi.org/10.1016/j.conbuildmat.2017.02.032.

Mohammadi, M., and Y.F. Wu. 2019. “Modified plastic-damage model for passively confined concrete based on triaxial tests.” Compos. Part B Eng., 159: 211–223. https://doi.org/10.1016/j.compositesb.2018.09.074.

Mostofinejad, D., N. Moshiri, and N. Mortazavi. 2015. “Effect of corner radius and aspect ratio on compressive behavior of rectangular concrete columns confined with CFRP.” Mater. Struct. Constr., 48 (1–2): 107–122. https://doi.org/10.1617/s11527-013-0171-9.

Nisticò, N. 2014. “R.C. square sections confined by FRP: A numerical procedure for predicting stress-strain relationships.” Compos. Part B Eng., 59: 238–247. https://doi.org/10.1016/j.compositesb.2013.12.004.

Nisticò, N., and G. Monti. 2013. “RC square sections confined by FRP: Analytical prediction of peak strength.” Compos. Part B Eng., 45 (1): 127–137. https://doi.org/10.1016/j.compositesb.2012.09.041.

Ozbakkaloglu, T. 2013. “Axial Compressive Behavior of Square and Rectangular High-Strength Concrete-Filled FRP Tubes.” J. Compos. Constr., 17 (1): 151–161. https://doi.org/10.1061/(ASCE)CC.1943-5614.0000321.

Ozbakkaloglu, T., and D. J. Oehlers. 2008. “Concrete-Filled Square and Rectangular FRP Tubes under Axial Compression.” J. Compos. Constr., 12 (4): 469–477. https://doi.org/10.1061/(asce)1090-0268(2008)12:4(469).

Papanikolaou, V. K., and A. J. Kappos. 2007. “Confinement-sensitive plasticity constitutive model for concrete in triaxial compression.” Int. J. Solids Struct., 44 (21): 7021–7048. https://doi.org/10.1016/j.ijsolstr.2007.03.022.

Pessiki, S., K. A. Harries, J. T. Kestner, R. Sause, and J. M. Ricles. 2001. “Axial Behavior of Reinforced Concrete Columns Confined with FRP Jackets.” J. Compos. Constr., 5 (4): 237–245. https://doi.org/10.1061/(ASCE)1090-0268(2001)5:4(237).

Piscesa, B., M. M. Attard, and A. K. Samani. 2016. “A lateral strain plasticity model for FRP confined concrete.” Compos. Struct., 158: 160–174. https://doi.org/10.1016/j.compstruct.2016.09.028.

Ribeiro, F., J. Sena-Cruz, F. G. Branco, and E. Júlio. 2019. “3D finite element model for hybrid FRP-confined concrete in compression using modified CDPM.” Eng. Struct., 190: 459–479. https://doi.org/10.1016/j.engstruct.2019.04.027.

Rochette, P., and P. Labossière. 2000. “Axial Testing of Rectangular Column Models Confined with Composites.” J. Compos. Constr., 4 (3): 129–136. https://doi.org/10.1061/(ASCE)1090-0268(2000)4:3(129).

Rousakis, T. C., A. I. Karabinis, P. D. Kiousis, and R. Tepfers. 2008. “Analytical modelling of plastic behaviour of uniformly FRP confined concrete members.” Compos. Part B Eng., 39 (7–8): 1104–1113. https://doi.org/10.1016/j.compositesb.2008.05.001.

Rudnicki, J. W., and J. R. Rice. 1975. “Conditions for the localization of deformation in pressure-sensitive dilatant materials.” J. Mech. Phys. Solids, 23 (6): 371–394. https://doi.org/10.1016/0022-5096(75)90001-0.

Saadatmanesh, H., M. R. Ehsani, and M. W. Li. 1994. “Strength and ductility of concrete columns externally reinforced with fiber composite straps.” ACI Struct. J., 91 (4): 434–447. https://doi.org/10.14359/4151.

Saleem, S., Q. Hussain, and A. Pimanmas. 2017. “Compressive Behavior of PET FRP–Confined Circular, Square, and Rectangular Concrete Columns.” J. Compos. Constr., 21 (3): 04016097. https://doi.org/10.1061/(asce)cc.1943-5614.0000754.

Samani, A. K., and M. M. Attard. 2014. “Lateral strain model for concrete under compression.” ACI Struct. J., 111 (2): 441–451. https://doi.org/10.14359/51686532.

Shahawy, M., A. Mirmiran, and T. Beitelman. 2000. “Tests and modeling of carbon-wrapped concrete columns.” Compos. Part B Eng., 31 (6–7): 471–480. https://doi.org/10.1016/S1359-8368(00)00021-4.

Shan, B., F. C. Gui, G. Monti, and Y. Xiao. 2019. “Effectiveness of CFRP Confinement and Compressive Strength of Square Concrete Columns.” J. Compos. Constr., 23 (6): 04019043. https://doi.org/10.1061/(asce)cc.1943-5614.0000967.

Sheikh, S. A., and S. M. Uzumeri. 1980. “Strength and Ductility of Tied Concrete Columns.” J. Struct. Div., 106 (5): 1079–1102. https://doi.org/10.1061/JSDEAG.0005416.

Simo, J. C., and R. L. Taylor. 1985. “Consistent tangent operators for rate-independent elastoplasticity.” Comput. Methods Appl. Mech. Eng., 48 (1): 101–118. https://doi.org/10.1016/0045-7825(85)90070-2.

Teng, J. G., Y. L. Huang, L. Lam, and L. P. Ye. 2007. “Theoretical Model for Fiber-Reinforced Polymer-Confined Concrete.” J. Compos. Constr., 11 (2): 201–210. https://doi.org/10.1061/(ASCE)1090-0268(2007)11:2(201).

Teng, J. G., T. Jiang, L. Lam, and Y. Z. Luo. 2009. “Refinement of a Design-Oriented Stress–Strain Model for FRP-Confined Concrete.” J. Compos. Constr., 13 (4): 269–278. https://doi.org/10.1061/(ASCE)CC.1943-5614.0000012.

Teng, J. G., and L. Lam. 2002. “Compressive Behavior of Carbon Fiber Reinforced Polymer-Confined Concrete in Elliptical Columns.” J. Struct. Eng., 128 (12): 1535–1543. https://doi.org/10.1061/(asce)0733-9445(2002)128:12(1535).

Teng, J. G., J. Y. Wu, S. Casalboni, Q. G. Xiao, and Y. Zhao. 2016. “Behavior and modeling of fiberreinforced polymer-confined concrete in elliptical columns.” Adv. Struct. Eng., 19 (9): 1359–1378. https://doi.org/10.1177/1369433216642122.

Teng, J. G., J. J. Zeng, and J. F. Chen. 2015a. “Measurement of axial stress distributions in FRP-confined concrete columns using TEKSCAN pressure sensors.” The 12th International Symposium on Fiber Reinforced Polymers for Reinforced Concrete Structures (FRPRCS-12) & The 5th Asia-Pacific Conference on Fiber Reinforced Polymers in Structures (APFIS-2015) Joint Conference. Nanjing, China.

Teng, J. G., Q. G. Xiao, T. Yu, and L. Lam. 2015b. “Three-dimensional finite element analysis of reinforced concrete columns with FRP and/or steel confinement.” Eng. Struct., 97: 15–28. https://doi.org/10.1016/j.engstruct.2015.03.030.

Wang, L.M., and Y.F. Wu. 2008. “Effect of corner radius on the performance of CFRP-confined square concrete columns: Test.” Eng. Struct., 30 (2): 493–505. https://doi.org/10.1016/j.engstruct.2007.04.016.

Wei, Y. Y., and Y. F. Wu. 2012. “Unified stress-strain model of concrete for FRP-confined columns.” Constr. Build. Mater., 26 (1): 381–392. Elsevier Ltd. https://doi.org/10.1016/j.conbuildmat.2011.06.037.

Wu, Y. F., and Y. Y. Wei. 2010. “Effect of cross-sectional aspect ratio on the strength of CFRP-confined rectangular concrete columns.” Eng. Struct., 32 (1): 32–45. https://doi.org/10.1016/j.engstruct.2009.08.012.

Yeh, F. Y., and K. C. Chang. 2012. “Size and shape effects on strength and ultimate strain in frp confined rectangular concrete columns.” J. Mech., 28 (4): 677–690. https://doi.org/10.1017/jmech.2012.118.

Yu, T., J. G. Teng, Y. L. Wong, and S. L. Dong. 2010a. “Finite element modeling of confined concrete-I: Drucker-Prager type plasticity model.” Eng. Struct., 32 (3): 665–679. https://doi.org/10.1016/j.engstruct.2009.11.014.

Yu, T., J. G. Teng, Y. L. Wong, and S. L. Dong. 2010b. “Finite element modeling of confined concrete-II: Plastic-damage model.” Eng. Struct., 32 (3): 680–691. https://doi.org/10.1016/j.engstruct.2009.11.013.

Zeng, L. F., G. Horrigmoe, and R. Andersen. 1996. “Numerical implementation of constitutive integration for rate-independent elastoplasticity.” Comput. Mech., 18 (5): 387–396. https://doi.org/10.1007/BF00376135.

Zheng, B. T., and J. G. Teng. 2022a. “A plasticity constitutive model for concrete under multiaxial compression.” Eng. Struct., 251 (PB): 113435. https://doi.org/10.1016/j.engstruct.2021.113435.

Zheng, B. T., and J. G. Teng. 2022b. “A 3D Plasticity Model for Concrete and Its Application to Concrete Under Non-uniform FRP Confinement.” In: 10th International Conference on FRP Composites in Civil Engineering (CICE 2021).

Appendix A Local axial stress measurements of an FRP-confined rectangular column in Teng et al. (2015a)

The tested column had a height of 332 mm, a cross-section of 133 mm × 166 mm, and a corner radius of 25 mm. The reported concrete properties of f_c = 42.5 MPa and ε_{co} = 0.0024 and the default values of E and ν were used in both the EPT and AA models. In addition, for the EPT model, the values of parameters ψ_k, $\bar{f}_t$, κ_s and ϱ_∞, which were determined by matching the section-average axial stress-strain predictions of three square columns with unpublished data provided by the authors of Teng et al. (2015a), are listed in Table A1.

The local axial stresses measured at a section-average stress level of 1.3 f_c were extracted from the data published in Teng et al. (2015a) and are compared with the FE predictions obtained with the EPT and AA models at two states (A and B). There are good reasons for the choice of different states in the AA predictions for comparison herein, with a section-average stress level of 1.3 f_c in the FE analysis being an obvious option as was adopted by Teng et al. (2015a). This obvious option was not taken for the comparisons herein as the axial stress-strain curve from the AA model was found to differ significantly from the experimental axial stress-strain curve. At state A, the axial strains from both models are equal to the axial strain corresponding to the 1.3 f_c stress level in the test data, which was found from unpublished section-average axial stress-strain curve of the column provided by the authors of Teng et al. (2015a). At state B, the maximum axial stresses (at the corner of the section) from both models are equal to the measured maximum axial stress over the section. Figure A1 compares the measured axial stresses with FE predictions along the three chosen paths over the section, and these paths are indicated in Figure A1. The measured axial stress distributions along the paths were directly obtained from the individual sensors along the paths as reported in Teng et al. (2015a), and the predicted axial stress distributions along the paths were obtained through 2D-interpolation of the FE results using the location of the three paths.

For the state A comparison for each path, the axial stresses are normalized by the maximum axial stress from the same source. The predictions from the two FE models generally agree with each other. Along path 2, the two sets of FE predictions show similar trends at state A (Figure A1b) but are very different from the measured results. However, they show a close match with the test data at state B (Figure A1e); the slight difference between the predicted and the measured peak stresses is due to the discrete load steps of the FE results. Along paths 1 and 3, the predictions from both FE models do not match the measured results well for both states. Further work is obviously necessary to achieve more robust and conclusive comparisons between FE predictions and measurement results for local axial stresses in FRP-confined concrete columns.

Tables

Table 1. FRP-confined non-circular columns simulated in the present study

Group	Specimen	Original name	Depth/major axis [mm]	Width/minor axis [mm]	Height [mm]	Corner radius [mm]	Number of FRP layers
Square columns (Wang and Wu 2008)	Sr0L1C31	C30-r0-1ply	150	150	300	0	1
	Sr15L1C31	C30-r15-1ply				15	1
	Sr0L2C53	C50-r0-2ply				0	2
	Sr15L2C53	C50-r15-2ply				15	2
	Sr30L2C53	C50-r30-2ply				30	2
	Sr60L2C53	C50-r60-2ply				60	2
Rectangular columns (Ozbakkaloglu 2013)	R1L3	A10R15L3	150	150	300	15	3
	R1L5	A10R15L5					5
	R1.5L3	A15R15L3	187.5	125			3
	R1.5L5	A15R15L5					5
	R2L3	A20R15L3	225	112.5			3
	R2L5	A20R15L5					5
Elliptical columns (Liu et al. 2022)	E1	E10A-L06-80	300	300	600	–	6
	E1.5	E15A-L06-80		200			
	E2	E20A-L06-80		150			
	E2.5	E25A-L06-80		120			

Table 2. Values of model parameters for square columns

Specimen	f_c[MPa]	ε_{co}	E[MPa]	κ_s/κ_c	ψ_k	$\bar{f}_t/f_c$	ϱ_∞	ν
Sr0L1C31 Sr15L1C31	31.0	0.0025	30900	10	0.6	0.10	0.6	0.18
Sr0L2C53 Sr15L2C53 Sr30L2C53 Sr60L2C53	53.0	0.0026	36200	10	1.2	0.14	0.6	0.18

Table 3. Values of model parameters for rectangular columns

Specimen	f_c[MPa]	ε_{co}	E[MPa]	κ_s/κ_c	ψ_k	$\bar{f}_t/f_c$	ϱ_∞	ν
R1L3 R1L5 R1.5L3 R1.5L5 R2L3 R2L5	77.9	0.0034	32600	8	0.6	0.10	0.6	0.18

Table 4. Values of model parameters for elliptical columns

Specimen	f_c[MPa]	ε_{co}	E[MPa]	κ_s/κ_c	ψ_k	$\bar{f}_t/f_c$	ϱ_∞	ν
E1 E1.5 E2 E2.5	41.2	0.0021	34200	8	0.8	0.14	0.6	0.185

Table 5. Default values of model parameters

Specimen	f_c[MPa]	ε_{co}	E[MPa]	κ_s/κ_c	ψ_k	$\bar{f}_t/f_c$	ϱ_∞	ν
Sr15L1C31	31.0	0.0019	26300	8	1.0	0.10	0.6	0.18
Sr15L2C53	53.0	0.0024	34400					
R1L3	77.9	0.0030	41700					
E2	41.2	0.0022	30300					

Table A1. Values of model parameters for the test column with measured local stresses

f_c[MPa]	ε_{co}	E[MPa]	κ_s/κ_c	ψ_k	$\bar{f}_t/f_c$	ϱ_∞	ν
42.5	0.0024	34200	10	1.2	0.14	0.8	0.18

Figure captions

Fig 1. Different stress paths during the pre- and post-transition stages: (a) stress-strain curves, (b) pre-transition path, (c) post-transition path.

Fig 2. Stress-strain curves of FRP-confined square columns: predictions versus test data from Wang and Wu (2008): (a) Sr0L1C31, (b) Sr0L2C53, (c) Sr15L1C31, (d) Sr15L2C53, (e) Sr30L2C53, (f) Sr60L2C53.

Fig 3. Axial stress distributions predicted with the EPT model for FRP-confined square columns of different corner radii: state A

Fig 4. Axial stress distributions predicted with the EPT model for FRP-confined square columns of different corner radii: state B

Fig 5. Axial stress distributions predicted with the EPT model for FRP-confined square columns of different corner radii: state C

Fig 6. Axial stress distributions predicted with the EPT and the AA models for FRP-confined square columns of different corner radii: state D

Fig 7. Confining and axial stresses in square sections with sharp and rounded corners: (a) principal confining stresses, (b) axial stress-axial strain curves.

Fig 8. Stress-strain curves of FRP-confined rectangular columns: predictions versus test data of Ozbakkaloglu (2013): (a) Specimens confined with 3 layers of FRP, (b) Specimens confined with 5 layers of FRP.

Fig 9. Axial stress distributions predicted with the EPT model for an FRP-confined rectangular columns of different aspect ratios at states A, B, and C

Fig 10. Axial stress distributions predicted with the EPT and the AA models for FRP-confined rectangular columns of different aspect ratios at state D

Fig 11. Confining and axial stresses in rectangular sections of different aspect ratios: (a) principal confining stresses, (b) axial stress-axial strain curves.

Fig 12. Stress-strain curves of FRP-confined elliptical columns: predictions versus test data of Liu et al. (2022): (a) EPT model, (b) AA model.

Fig 13. Axial stress distributions predicted with the EPT and the AA models for FRP-confined elliptical columns of different aspect ratios at state D

Fig 14. Confining and axial stresses in elliptical sections with different aspect ratios: (a) principal confining stresses, (b) axial stress-axial strain curves.

Fig A1. Axial stress distributions along three paths of an FRP-confined rectangular column: predictions versus test data of Teng et al. (2015a): (a) Path 1, state A, (b) Path 2, state A, (c) Path 3, state A, (d) Path 1, state B, (e) Path 2, state B, (f) Path 3, state B.

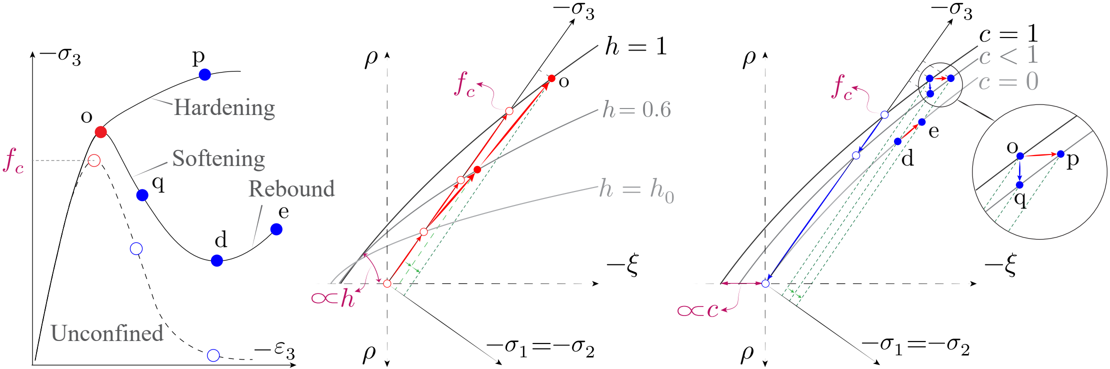

(a) Stress-strain (b) Pre-transition (c) Post-transition

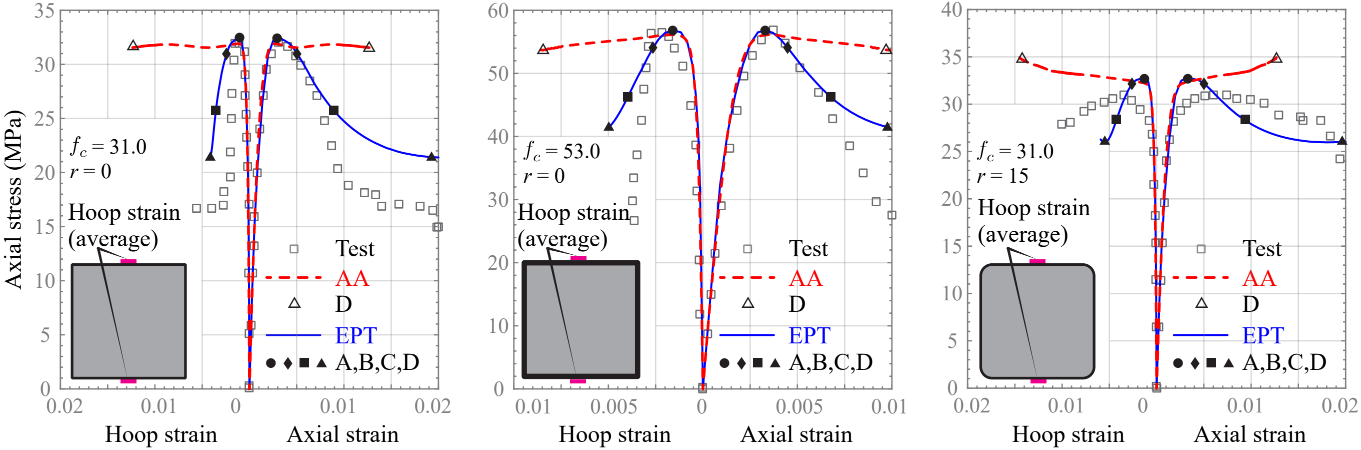

(a) Sr0L1C31 (b) Sr0L2C53 (c) Sr15L1C31

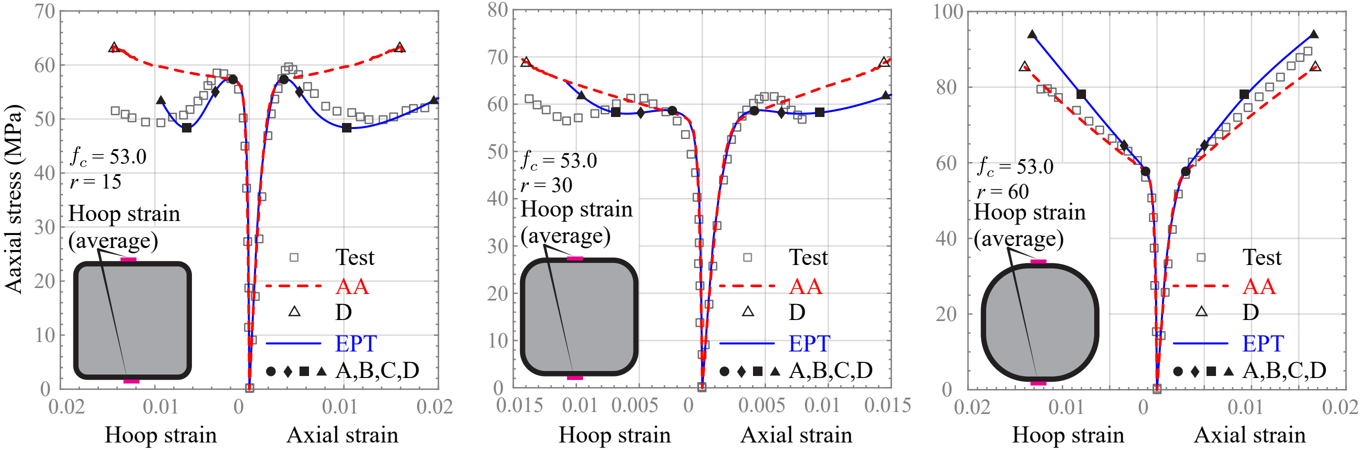

(d) Sr15L2C53 (e) Sr30L2C53 (f) Sr60L2C53

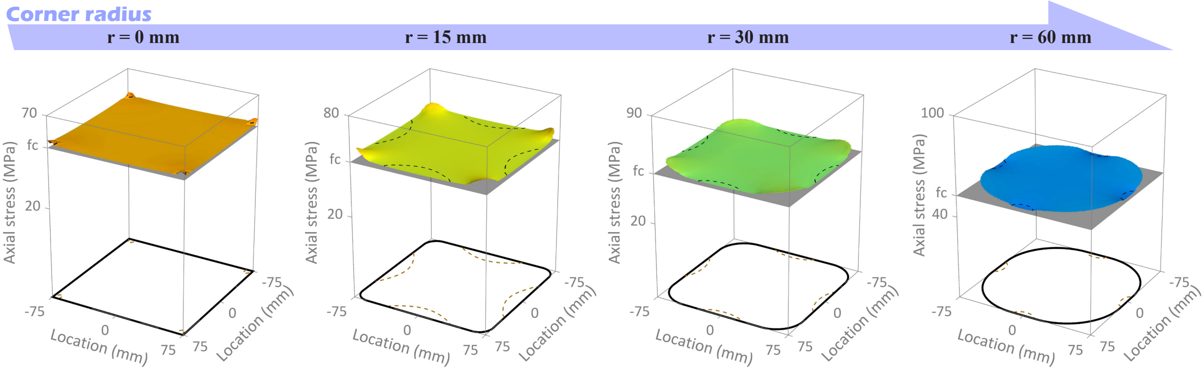
Corner radius
r = 0 mm
r = 15 mm
r = 30 mm
r = 60 mm
Axial stress (MPa)
70
fc
20
80
fc
20
90
fc
20
100
fc
40
Location (mm)
-75
0
75
Location (mm)
-75
0
75

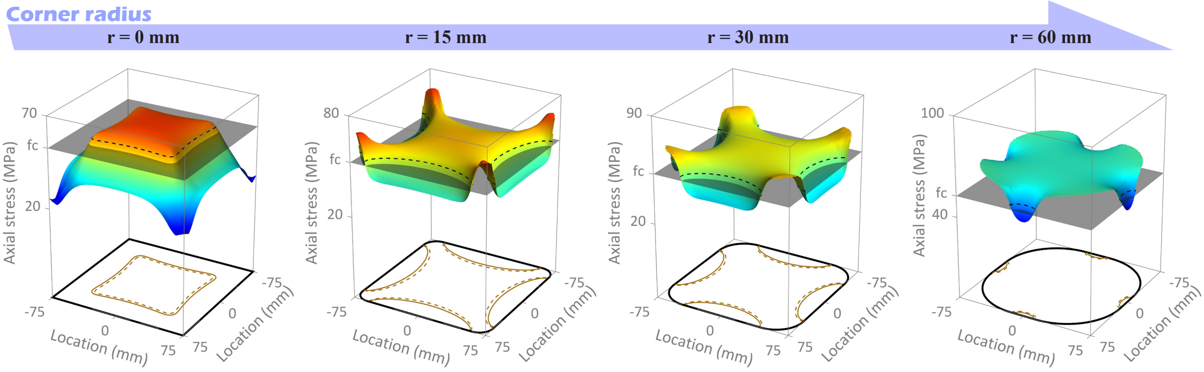
Corner radius
r = 0 mm
r = 15 mm
r = 30 mm
r = 60 mm
70
fc
20
Axial stress (MPa)
-75
0
75
Location (mm)
75
0
-75
Location (mm)
80
fc
20
Axial stress (MPa)
-75
0
75
Location (mm)
75
0
-75
Location (mm)
90
fc
20
Axial stress (MPa)
-75
0
75
Location (mm)
75
0
-75
Location (mm)
100
fc
40
Axial stress (MPa)
-75
0
75
Location (mm)
75
0
-75
Location (mm)

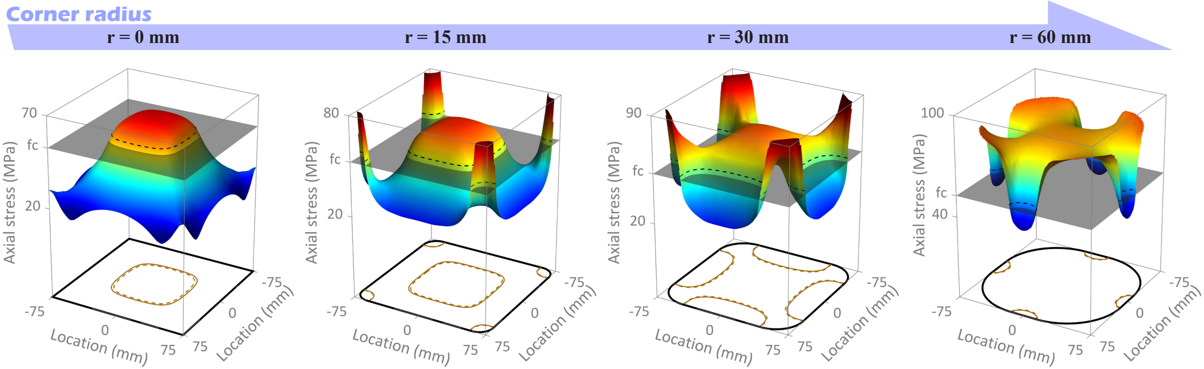

Corner radius
r = 0 mm
r = 15 mm
r = 30 mm
r = 60 mm
Axial stress (MPa)
70
fc
20
80
fc
20
90
fc
20
100
fc
40
Location (mm)
-75
0
75
Location (mm)
-75
0
75

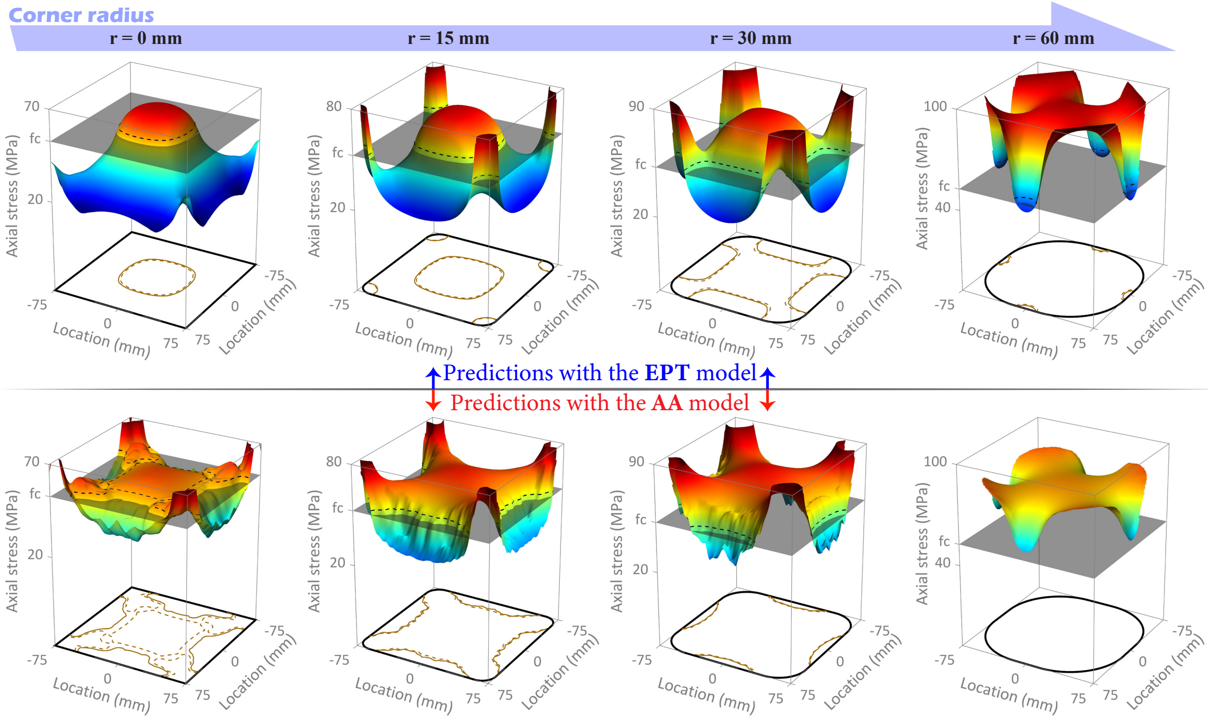
Corner radius
r = 0 mm
r = 15 mm
r = 30 mm
r = 60 mm
Predictions with the **EPT** model
Predictions with the **AA** model
Axial stress (MPa)
70
80
90
100
fc
20
40
Location (mm)
-75
0
75

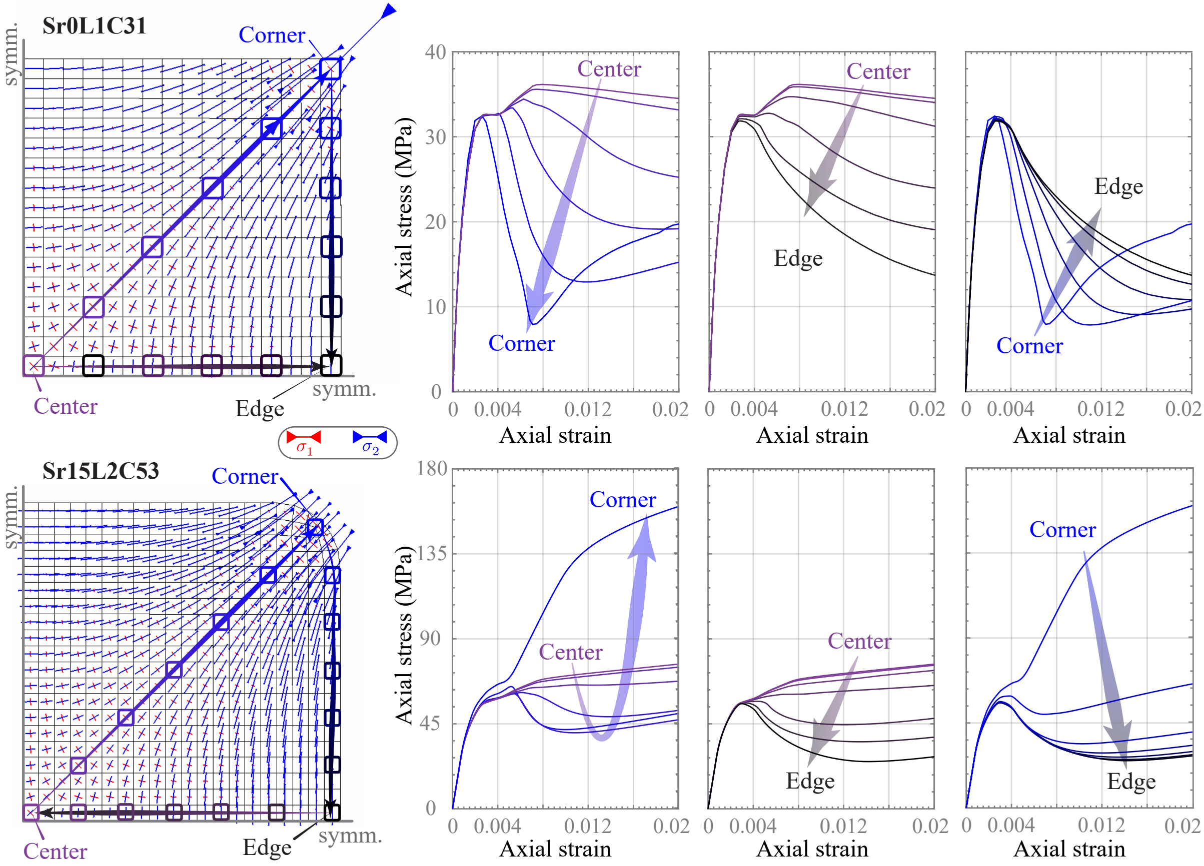

(a) Principal confining stresses

(b) Axial stress-axial strain curves

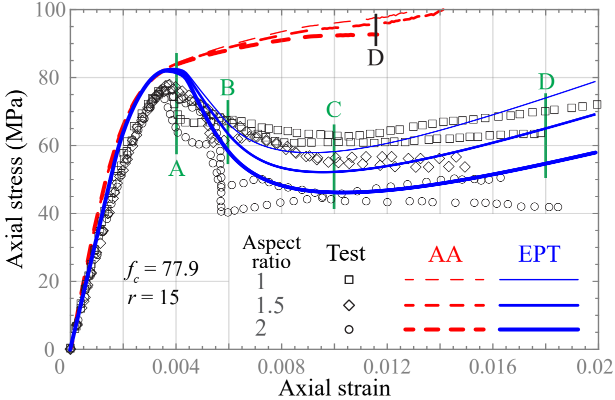

(a) L3 specimens

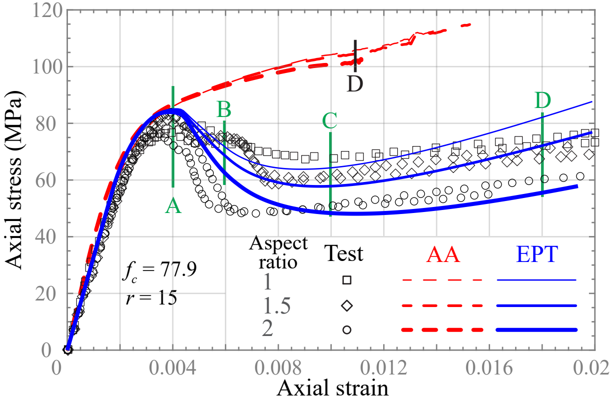

(b) L5 specimens

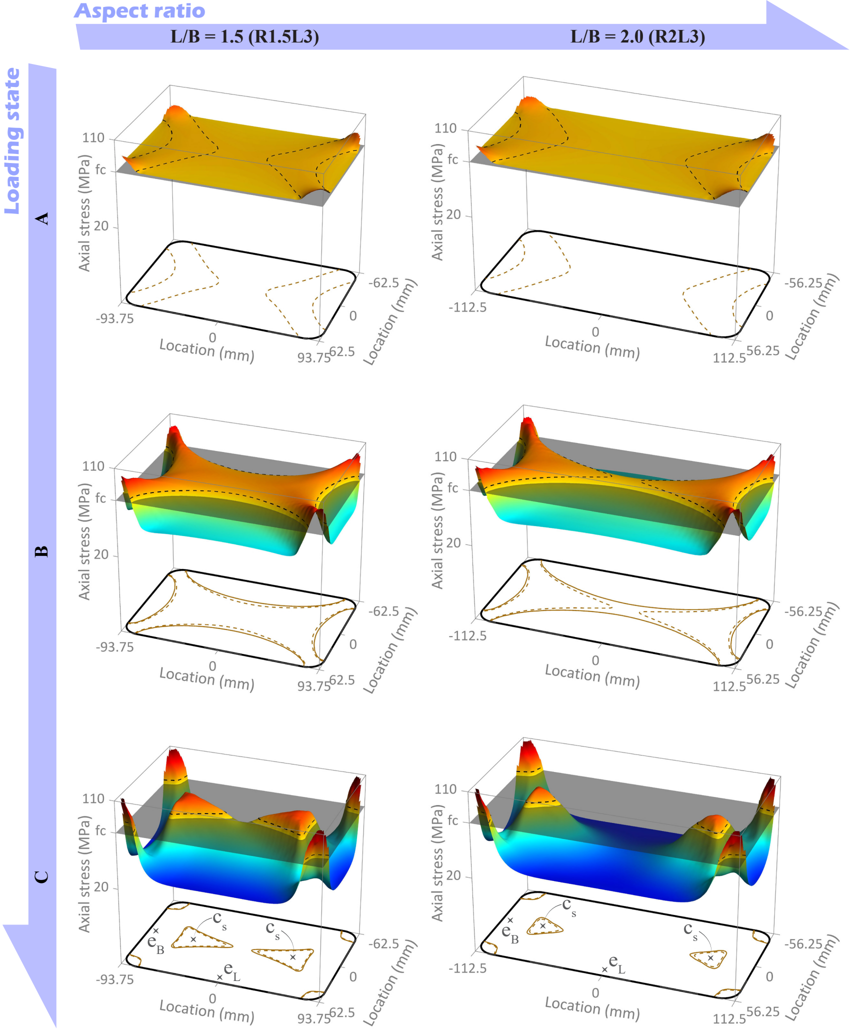
Aspect ratio
L/B = 1.5 (R1.5L3)
L/B = 2.0 (R2L3)
Loading state
A
B
C
Axial stress (MPa)
110
fc
20
Location (mm)
-93.75
0
93.75
-62.5
0
62.5
-112.5
112.5
-56.25
56.25
c_s
e_B
e_L

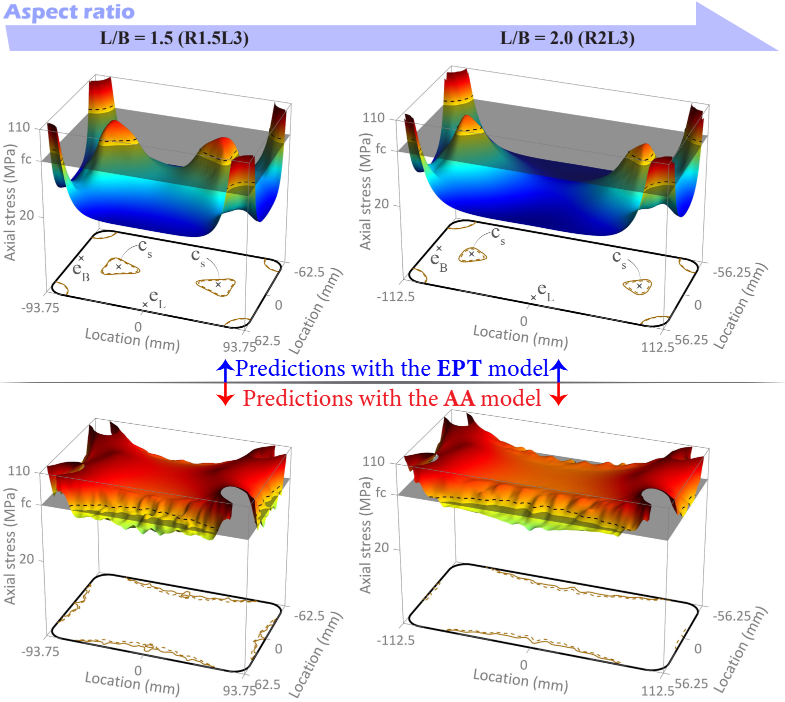

Aspect ratio
L/B = 1.5 (R1.5L3)
L/B = 2.0 (R2L3)
110
fc
20
Axial stress (MPa)
c s
c s
e B
e L
-93.75
0
93.75
Location (mm)
-62.5
0
62.5
Location (mm)
110
fc
20
Axial stress (MPa)
c s
c s
e B
e L
-112.5
0
112.5
Location (mm)
-56.25
0
56.25
Location (mm)
Predictions with the EPT model
Predictions with the AA model
110
fc
20
Axial stress (MPa)
-93.75
0
93.75
Location (mm)
-62.5
0
62.5
Location (mm)
110
fc
20
Axial stress (MPa)
-112.5
0
112.5
Location (mm)
-56.25
0
56.25
Location (mm)

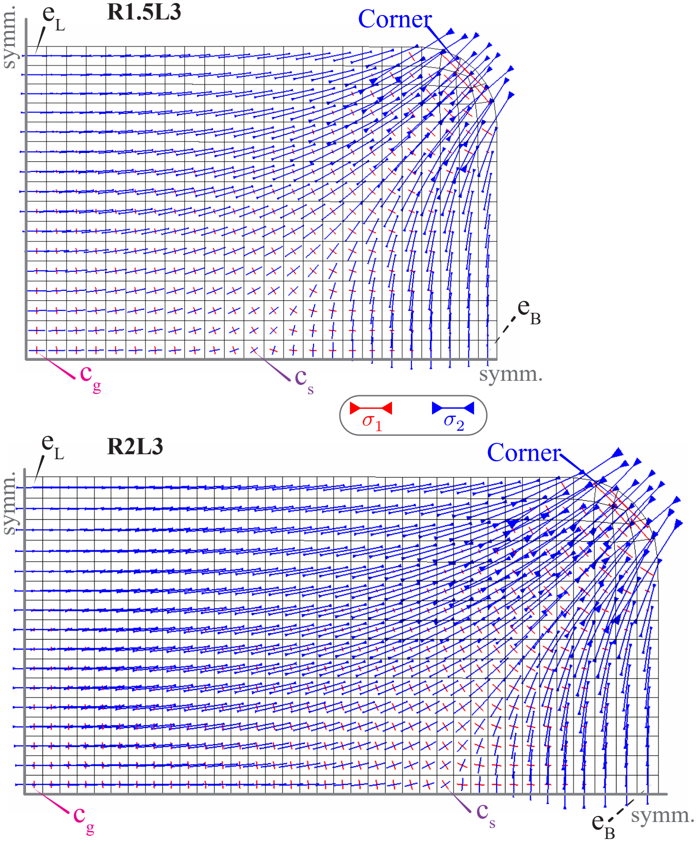

(a) Principal confining stresses

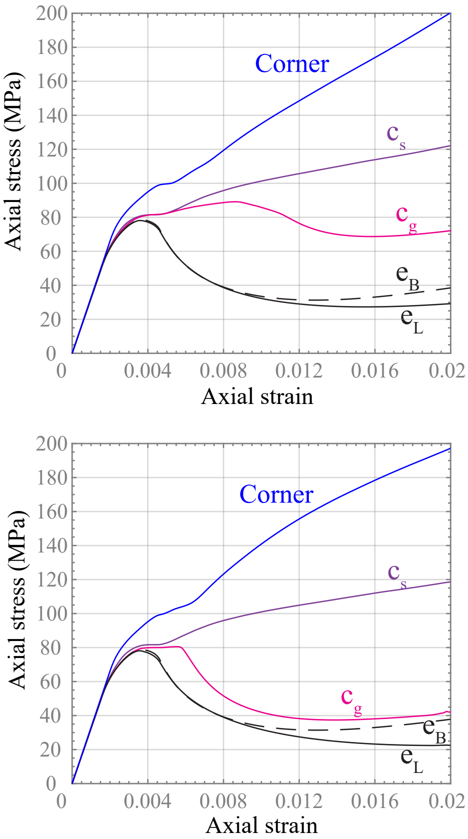

(b) Axial stress-axial strain curves

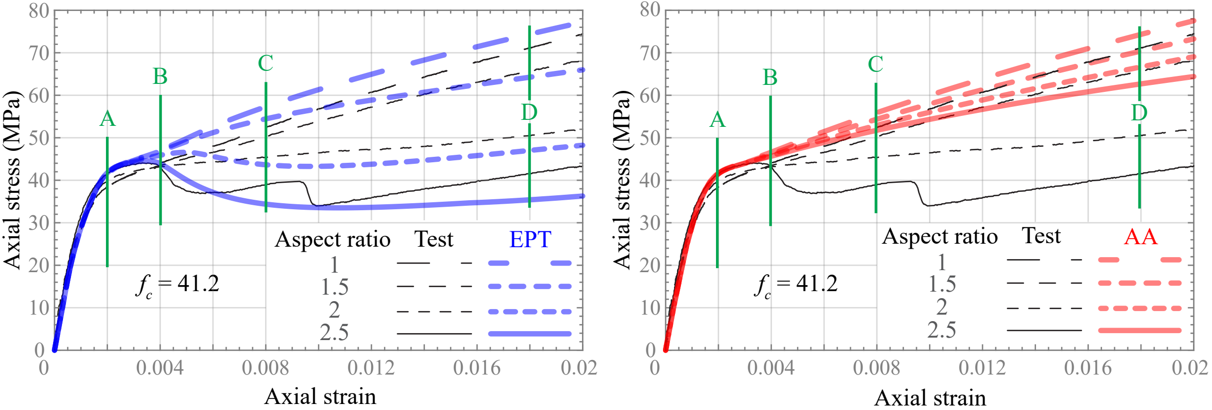
Axial stress (MPa)
80
70
60
50
40
30
20
10
0
0
0.004
0.008
0.012
0.016
0.02
Axial strain
A
B
C
D
$f_c = 41.2$
Aspect ratio
Test
EPT
1
1.5
2
2.5
Axial stress (MPa)
Axial strain
A
B
C
D
$f_c = 41.2$
Aspect ratio
Test
AA
1
1.5
2
2.5

(a) EPT

(b) AA

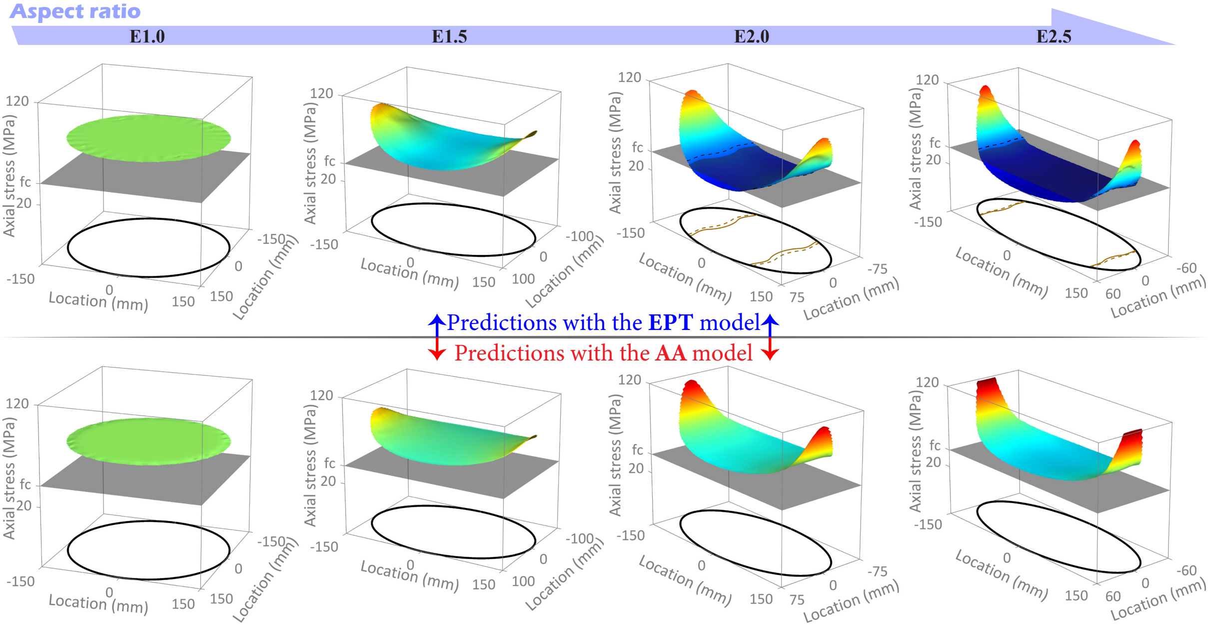
Aspect ratio
E1.0
E1.5
E2.0
E2.5
Axial stress (MPa)
120
fc
20
-150
Location (mm)
0
150
-150
-100
100
-75
75
-60
60
Predictions with the EPT model
Predictions with the AA model

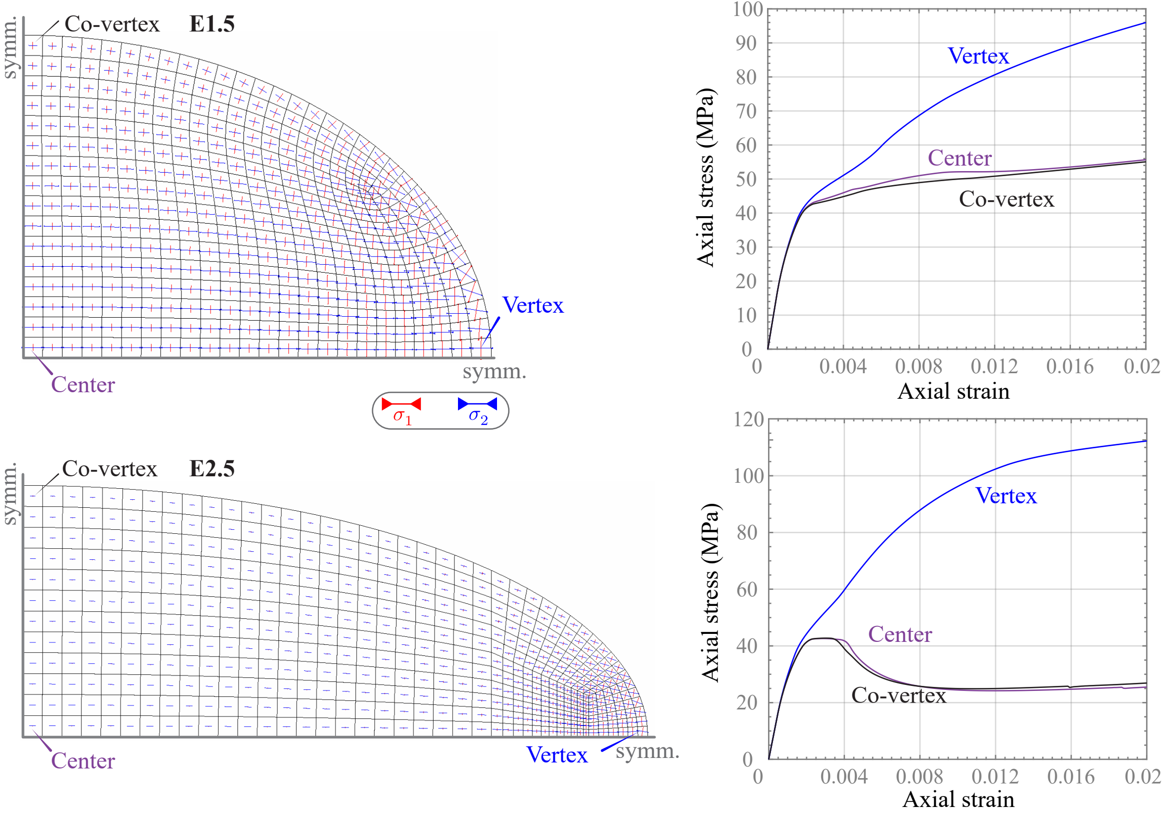

(a) Principal confining stresses

(b) Axial stress-axial strain curves